Methods for Computing Accurate Atomic Spin Moments for Collinear and Noncollinear Magnetism in Periodic and Nonperiodic Materials

Thomas A. Manz* and David S. Sholl*

School of Chemical and Biomolecular Engineering, Georgia Institute of Technology, 311 Ferst Drive N.W., Atlanta, Georgia 30332-0100, United States

Ⓢ *Supporting Information*

ABSTRACT: The partitioning of electron spin density among atoms in a material gives atomic spin moments (ASMs), which are important for understanding magnetic properties. We compare ASMs computed using different population analysis methods and introduce a method for computing density derived electrostatic and chemical (DDEC) ASMs. Bader and DDEC ASMs can be computed for periodic and nonperiodic materials with either collinear or noncollinear magnetism, while natural population analysis (NPA) ASMs can be computed for nonperiodic materials with collinear magnetism. Our results show Bader, DDEC, and (where applicable) NPA methods give similar ASMs, but different net atomic charges. Because they are optimized to reproduce both the magnetic field and the chemical states of atoms in a material, DDEC ASMs are especially suitable for constructing interaction potentials for atomistic simulations. We describe the computation of accurate ASMs for (a) a variety of systems using collinear and noncollinear spin DFT, (b) highly correlated materials (e.g., magnetite) using DFT+U, and (c) various spin states of ozone using coupled cluster expansions. The computed ASMs are in good agreement with available experimental results for a variety of periodic and nonperiodic materials. Examples considered include the antiferromagnetic metal organic framework $Cu_3(BTC)_2$, several ozone spin states, mono- and binuclear transition metal complexes, ferri- and ferro-magnetic solids (e.g., Fe_3O_4, Fe_3Si), and simple molecular systems. We briefly discuss the theory of exchange-correlation functionals for studying noncollinear magnetism. A method for finding the ground state of systems with highly noncollinear magnetism is introduced. We use these methods to study the spin−orbit coupling potential energy surface of the single molecule magnet $Fe_4C_{40}H_{52}N_4O_{12}$, which has highly noncollinear magnetism, and find that it contains unusual features that give a new interpretation to experimental data.

1. INTRODUCTION

Common sources of magnetism in materials include unpaired electrons, nuclear spins, orbital moments, and electric currents. Here, we focus on the magnetic field component $\vec{B}^{spin}(\vec{r})$ due to unpaired electrons. In chemical systems containing unpaired electrons, the assignment of an atomic spin moment (ASM) to each atom serves several important purposes. First, this helps quantify the type of magnetic state (ferromagnetic, antiferromagnetic, ferrimagnetic, etc.) of a material. By allowing one to theoretically study atomistic changes in magnetism as a function of chemical composition, ASMs facilitate the understanding of existing materials and the design of new materials. ASMs computed from quantum chemistry calculations can be used to develop interaction potentials for atomistic simulations of magnetism that facilitate the study of larger systems and statistical ensembles. For example, atomistic simulations using Ising and other lattice-based models have been used to study magnetic phase transitions, magnetic domain boundaries, spin spirals, and other complex phenomena.[1−3] To serve all of these purposes, ASMs should be simultaneously optimized to reproduce $\vec{B}^{spin}(\vec{r})$ and the chemical states of atoms in a material. Here, we describe how ASMs optimized for these uses can be computed from the spin density of a quantum chemistry calculation. We compare these results to both experimental data and other methods for computing ASMs.

Common methods for computing ASMs include Hirshfeld, Mulliken, natural, and Bader population analysis.[4−10] Integrating the total spin density within an effective atomic sphere radius is another common method for computing ASMs, but this has the disadvantage that regions between atomic spheres are not assigned to any atom, so the ASMs do not sum to the total spin moment of the unit cell.[11] The Hirshfeld method is known to give net atomic charges (NACs) too small in magnitude.[12−14] Basis set sensitivity is a key disadvantage of Mulliken population analysis.[7,8] Because of these well-documented problems, we do not consider Hirshfeld and Mulliken analysis further in this article. Natural population analysis (NPA) addresses the basis set issue,[7,8] but it is not readily available for periodic systems or noncollinear magnetism. In some cases, Mulliken populations can also be stabilized by projection onto a minimal basis set (MBS).[8,15] Bader analysis partitions space into nonoverlapping atomic volumes and assigns all of the spin density within an atomic volume to that atom.[4,5,9] Bader analysis does not directly depend on the basis set and can be readily applied to periodic and nonperiodic systems with collinear or noncollinear magnetism. Although Bader NACs are chemically meaningful, they do not accurately reproduce the electrostatic potential, $V(\vec{r})$, outside the electron distribution, which limits their use for force-field development.[14] As shown in the Results below, the NPA and Bader methods give reliable ASMs.

Previously, we introduced density derived electrostatic and chemical (DDEC) charges that are simultaneously optimized to reproduce both the chemical states of atoms and $V(\vec{r})$ outside a material's electron distribution, which makes them suitable for use in force fields and for studying electron transfer during chemical reactions.[14] DDEC NACs have been used to model gas adsorption in metal organic frameworks and to quantify the amount of charge transfer in molecular zippers.[16,17] Here, we extend the DDEC method to the computation of ASMs in both collinear and noncollinear magnetism. The DDEC NACs and ASMs are self-consistently derived from the same atomic charge density distributions. These ASMs are simultaneously optimized to reproduce $\vec{B}^{spin}(\vec{r})$ and the chemical states of atoms in a material, which makes them especially suitable for use in force fields and for interpreting material properties.

The electron spin density can be described using a four-component spinor, whose four charge density components are directly related to the total electron density, $\rho(\vec{r})$, and the spin magnetization density, $\vec{m}(\vec{r})$. Either the Dirac spinor or the Pauli spin matrices can be used to describe this spinor.[18−20] To make our method equally applicable for either spin formulation, we use $\rho(\vec{r})$ and $\vec{m}(\vec{r})$ directly. The operator for measuring the spin of electron j is

$$\vec{s}(j) = \hat{x}s_x(j) + \hat{y}s_y(j) + \hat{z}s_z(j) \tag{1}$$

where $s_x(j)$, $s_y(j)$, and $s_z(j)$ are the operators for measuring its spin along the $\hat{x}$, $\hat{y}$, and $\hat{z}$ directions, respectively.[21] Here, we denote the magnitude and direction of a vector by $b = |\vec{b}|$ and $\hat{b} = \vec{b}/b$, respectively. We use δ^{dirac} to denote the Dirac delta function and δ to denote a variational derivative. For a system containing N electrons, the spin magnetization density, $\vec{m}(\vec{r})$, can be computed by summing the spins of all electrons at position $\vec{r}$ and dividing by the spin magnitude of an individual electron. Specifically,

$$\vec{m}(\vec{r}) = 2\langle\Psi| \sum_{j=1}^{N} (\vec{s}(j)\delta^{dirac}(\vec{r} - \vec{e}_j))|\Psi\rangle \tag{2}$$

where $\Psi(\{\vec{e}_j\})$ is the multielectronic wave function and $\{\vec{e}_j\}$ are the spatial coordinates of the electrons. The factor of 2 occurs because the spin magnitude of an individual electron is one-half. Spin can be measured along any unit direction $\hat{h}$, and the value of the spin density projected onto a measurement direction $\hat{h}$ is

$$\rho(\vec{r}, \hat{h}) = (\rho(\vec{r}) + \vec{m}(\vec{r})\cdot\hat{h})/2 \tag{3}$$

where $\rho(\vec{r})$ and $\vec{m}(\vec{r})$ are expressed in units of electrons per unit volume.[22] Collinear magnetism occurs when $\hat{m}(\vec{r})$ is parallel to a global magnetization axis, $\hat{h}_{global}$, while noncollinear magnetism occurs when it is not. Collinear magnetism has only two independent electron density components, $\rho^{\alpha}(\vec{r})$ and $\rho^{\beta}(\vec{r})$, which are the spin density projected onto measurement directions $\hat{h}_{global}$ and $-\hat{h}_{global}$, respectively.

Since the nonrelativistic and scalar-relativistic Hamiltonians of a chemical system commute with the spin measurement operators, energy eigenstates can be represented as spin eigenstates.[21] When, however, relativistic spin coupling interactions (e.g., spin−orbit coupling,[23] spin−spin coupling,[24] or a nonuniform magnetic field[25]) are added, the spin measurement operators may no longer commute with the Hamiltonian, leading to energy eigenstates that are not spin eigenstates.[23−25] We now discuss the theory of spin eigenstates, called pure spin states, for nonperiodic systems.

The multielectronic spin operator, $\vec{S}$, for a nonperiodic system containing N electrons is[21]

$$\vec{S} = \sum_{j=1}^{N} \vec{s}(j) \tag{4}$$

Spin eigenstates are described by two quantum numbers and a spin direction.[21,26] The first spin quantum number (S) satisfies the relationship[21]

$$\vec{S}\cdot\vec{S}|\Psi\rangle = (S(S + 1))|\Psi\rangle \tag{5}$$

Since s_x, s_y, and s_z do not commute, eigenstates along one spin direction are not eigenstates along another spin direction.[21,26] For the purpose of preparing an orthonormal set of spin eigenstates, the spin direction is conventionally chosen to be $\hat{z}$.[21,26] The second spin quantum number (S_z) is the net spin projected onto the spin direction:

$$S_z = \frac{1}{2}\oint \vec{m}(\vec{r})\cdot\hat{z}\, d^3\vec{r} \tag{6}$$

where the closed integral symbol indicates integration over a domain without boundary, and since eq 6 is a volume integral this denotes integration over all positions in space. For a spin eigenstate[21]

$$\vec{S}\cdot\hat{z}|\Psi\rangle = S_z|\Psi\rangle \tag{7}$$

The allowable eigenstates for S_z are

$$S_z \in \{-S, (-S + 1), ...S\} \tag{8}$$

giving a spin multiplicity of $2S + 1$.[21,26] In the absence of spin coupling interactions, these $2S + 1$ states are degenerate. The value of S is (a) 0 for singlet states, (b) 1/2 for doublet states, (c) 1 for a triplet states, etc. The descriptor

$$\Delta_S = \langle\Psi|\vec{S}\cdot\vec{S}|\Psi\rangle - S(S + 1) \tag{9}$$

is useful for quantifying the amount of spin contamination in nonperiodic systems, where $\Delta_S = 0$ for a pure spin state.[27,28] The situation for periodic materials is more complicated, particularly because the spin structure may not have the periodicity of the ionic structure, leading to phenomena such as spin density waves and frustrated magnetism.[29−33] For all systems studied in this paper except the single molecule magnet with noncollinear magnetism and spin−orbit coupling, the energy eigenstates should be spin eigenstates.

Several factors need to be considered when computing spin densities using spin density functional theory (DFT).[34] For the hypothetically exact exchange-correlation (XC) functional, DFT gives the wave function of a fictitious noninteracting system whose energy, $\rho(\vec{r})$, and $\vec{m}(\vec{r})$ are the same as in the real interacting system.[35] Since ASMs are directly derived from $\rho(\vec{r})$ and $\vec{m}(\vec{r})$, the DFT wave function computed from the exact XC functional would give the same ASMs as the wave function of the real interacting system. The DFT wave function of the noninteracting system need not be a spin eigenstate, even though it formally reproduces the spin densities of the real interacting system.[34,36] In practice, systems for which the DFT wave function has a small (large) amount of spin contamination are easier (harder) to accurately model. For this reason, we present and discuss Δ_S values for the nonperiodic DFT wave functions in the Results below. One must be particularly careful when using DFT to compute the spin densities of multireference systems

like open shell singlets and states for which $|S_z| < S$, since the symmetry of the spin density may not be well-represented by a single Slater determinant.[37−40] Extensions of DFT using a linear combination of Slater determinants have been developed to handle these difficult cases and to approximately treat excited states.[37,41−44]

In this article, we focus mainly on nonrelativistic and scalar-relativistic Hamiltonians where energy eigenstates should in principle be representable as spin eigenstates. We study a variety of periodic and nonperiodic collinear magnetic systems using traditional DFT methods, including a DFT+U and range-separated hybrid study of the charge-spin ordering in bulk magnetite. We use coupled-cluster expansions to study various spin states of ozone. Coupled cluster methods that give formally exact expansions of the system's wave function within the nonrelativistic and scalar-relativistic Born−Oppenheimer approximations are a useful and powerful tool for modeling multireference systems.[45−49] In addition, a noncollinear single molecule magnet is studied using noncollinear DFT including spin−orbit coupling interactions. Several population analysis methods are applied to each of these systems. In agreement with prior literature, we find the choice of population analysis method has a smaller effect on the computed ASMs than on the computed NACs.[50] We find the DDEC method described in this article gives reliable NACs and ASMs for all the materials studied.

The rest of this paper is organized as follows. Section 2 describes a theory for partitioning the spin density among atoms in a material to give ASMs that simultaneously reproduce the chemical states of atoms and $\vec{B}^{\text{spin}}(\vec{r})$ outside the material's electron distribution. Section 2 also describes the theory of choosing an appropriate XC functional for modeling different types of noncollinear magnetism. Section 3 describes the computational methods used to compute optimized geometries, electron density distributions, NACs, and ASMs. In section 4, we use these methods to study a variety of periodic and nonperiodic materials with collinear and noncollinear magnetism. We describe the main conclusions of this work in section 5. The Appendix proves that the optimization functional for computing ASMs converges to a unique solution and also contains algorithms for computing a function and constant used in the iterative solution method.

2. THEORY

2.1. Atom-in-Molecules (AIM) Formalism. This section describes universal equations for partitioning the total spin density among atoms in a material, for computing ASMs from atomic spin density distributions, for expressing $\vec{B}^{\text{spin}}(\vec{r})$ as a distributed multipole expansion, and for quantifying how accurately a set of ASMs reproduce $\vec{B}^{\text{spin}}(\vec{r})$. These equations apply to all atoms-in-molecule methods. We begin by defining an arbitrary material as a set of atoms {A} at positions {$\vec{R}_A$}, in a reference unit cell, $\mathbf{U}$.[14] For a nonperiodic system (e.g., a molecule), $\mathbf{U}$ is any parallelpiped enclosing the entire electron distribution. Using this notation, $\vec{m}(\vec{r})$ can be written as a sum of atomic spin magnetization densities

$$\vec{m}(\vec{r}) = \vec{\Delta}(\vec{r}) + \sum_{k,A} \vec{m}_A(\vec{r}_A) \tag{10}$$

where the constraint

$$\vec{\Delta}(\vec{r}) = \vec{0} \tag{11}$$

will be imposed below using a Lagrange multiplier. Throughout this article, we use the short-hand notation

$$\sum_{k,A} = \sum_{k_1} \sum_{k_2} \sum_{k_3} \sum_A \tag{12}$$

The reference unit cell has $k_1 = k_2 = k_3 = 0$ and summation over A means summation over all atoms in this unit cell. For a periodic direction, k_i ranges over all integers with the associated lattice vector $\vec{v}_i$. For a nonperiodic direction, $k_i = 0$ and $\vec{v}_i$ is the corresponding edge of $\mathbf{U}$. Using this notation, the vector and distance relative to atom A are given by

$$\vec{r}_A = \vec{r} - k_1 \vec{v}_1 - k_2 \vec{v}_2 - k_3 \vec{v}_3 - \vec{R}_A \tag{13}$$

and $r_A = |\vec{r}_A|$.[14] Analogous to eq 3, the value of the atomic spin density projected onto a measurement direction $\hat{h}$ is

$$\rho_A(\vec{r}_A, \hat{h}) = (\rho_A(\vec{r}_A) + \vec{m}_A(\vec{r}_A) \cdot \hat{h})/2 \tag{14}$$

The atomic electron distribution, $\rho_A(\vec{r}_A)$, is computed via an atoms-in-molecule (AIM) formalism such as Bader,[4,5] DDEC,[14] Hirshfeld,[6] iterative Hirshfeld,[12] or iterative Stockholder atom[51] analysis.

The ASM is the vector $\vec{M}_A$ computed by integrating $\vec{m}_A(\vec{r}_A)$,

$$\vec{M}_A = \oint \vec{m}_A(\vec{r}_A)\, \mathrm{d}^3\vec{r}_A \tag{15}$$

For collinear magnetism, the ASM can be equivalently expressed as the scalar projection of $\vec{M}_A$ onto the global spin quantization axis:

$$T_A = \vec{M}_A \cdot \hat{h}_{\text{global}} \tag{16}$$

The unit cell spin moment, $\vec{M}$, is the sum of individual ASMs,

$$\vec{M} = \sum_A \vec{M}_A \tag{17}$$

For collinear magnetism, the unit cell spin moment can be equivalently expressed as the scalar projection of $\vec{M}$ onto the global spin quantization axis:

$$T = \vec{M} \cdot \hat{h}_{\text{global}} = \sum_A T_A \tag{18}$$

Since the spin-derived magnetic moment of a spin-up electron is $g_e \mu_B/2$ where $g_e \approx -2.002319$ is the electron's g factor and μ_B is the Bohr magneton,[52] all spin-derived magnetic moments in this paper are reported in units of $g_e \mu_B/2$. (Because of its negative charge, the electron's spin and magnetic moments point in opposite directions, causing g_e to be negative.) In these units, each electron contributes unit magnitude. For collinear systems, T_A is the number of spin-up minus spin-down electrons assigned to atom A, and T is the number of spin-up minus spin-down electrons in the unit cell.

Subject to the above constraints, the key issue is how to optimize {$\vec{m}_A(\vec{r}_A)$} to simultaneously reproduce $\vec{B}^{\text{spin}}(\vec{r})$ and the chemical states of atoms. An atomic expansion of $\vec{B}^{\text{spin}}(\vec{r})$ has the form

$$\vec{B}^{\text{spin}}(\vec{r}) = \sum_{k,A} \vec{B}_A^{\text{spin}}(\vec{r}_A) \tag{19}$$

We assume the wave function and other properties are not time-dependent. Setting the density of point magnetic dipoles equal to $g_e \mu_B \vec{m}_A(\vec{r}'_A)/2$ and integrating the classical expression for the

magnetic field of a point dipole[52,53] over $\vec{r}'_A$ gives

$$
\begin{aligned}
&\vec{B}_A^{\text{spin}}(\vec{r}_A) \\
&= \frac{\mu_0}{4\pi}\left(\frac{g_e\mu_B}{2}\right)\oint\left(\frac{3(\vec{r}_A - \vec{r}'_A)(\vec{m}_A(\vec{r}'_A)\cdot(\vec{r}_A - \vec{r}'_A))}{|\vec{r}_A - \vec{r}'_A|^5}\right. \\
&\quad\left. - \frac{\vec{m}_A(\vec{r}'_A)}{|\vec{r}_A - \vec{r}'_A|^3}\right)\,\mathrm{d}^3\vec{r}'_A
\end{aligned}
\tag{20}
$$

One can rewrite eq 20 with the help of a multipolar expansion as

$$
\vec{B}_A^{\text{spin}}(\vec{r}_A) = \frac{\mu_0}{4\pi}\left(\frac{g_e\mu_B}{2}\right)\left(\frac{3\vec{r}_A(\vec{M}_A\cdot\vec{r}_A)}{(r_A)^5} - \frac{\vec{M}_A}{(r_A)^3}\right) + Q_A + P_A
\tag{21}
$$

where magnetic dipoles are the leading term. The terms Q_A and P_A are due to higher order magnetic multipoles and electron cloud penetration effects, respectively. The penetration term P_A is essentially zero for r_A values greater than a critical radius where $\rho_A(\vec{r}_A)$ is negligible. For the development of force fields, it is convenient to choose values for $\{\vec{M}_A\}$ such that Q_A is small for large distances where P_A is negligible. Under these conditions, $\vec{B}^{\text{spin}}(\vec{r})$ can be accurately reproduced using just the $\{\vec{M}_A\}$ values, which facilitates constructing a force field to reproduce $\vec{B}^{\text{spin}}(\vec{r})$. Due to symmetry, Q_A is zero when $\vec{m}_A(\vec{r}_A)$ is spherically symmetric, that is, when $\vec{m}_A(\vec{r}_A) = \vec{m}_A^{\text{avg}}(r_A)$. Thus, to simultaneously reproduce an atom's chemical state and $\vec{B}_A^{\text{spin}}(\vec{r}_A)$ for large r_A values, $\vec{m}_A(\vec{r}_A)$ should be optimized to resemble $\vec{m}_A^{\text{avg}}(r_A)$ subject to constraint 26, where the spherical average $g_A^{\text{avg}}(r_A)$ of a scalar or vector field $g_A(\vec{r}_A)$ is defined by

$$
g_A^{\text{avg}}(r_A) = \frac{1}{4\pi(r_A)^2}\oint g_A(\vec{r}'_A)\delta^{\text{dirac}}(r_A - r'_A)\,\mathrm{d}^3\vec{r}'_A
\tag{22}
$$

The potential energy of a charge, q, and magnetic dipole, $\vec{M}$, placed in an electrostatic potential $V(\vec{r})$ and magnetostatic field $\vec{B}(\vec{r})$ is

$$
E = qV(\vec{r}) - \vec{M}\cdot\vec{B}(\vec{r})
\tag{23}
$$

Thus, to obtain the most accurate energies in atomistic simulations, NACs and ASMs should be optimized to reproduce $V(\vec{r})$ and $\vec{B}^{\text{spin}}(\vec{r})$ outside a material's van der Waals surface. For time-independent fields, such as those considered here, $V(\vec{r})$ is determined up to an additive constant, and $\vec{B}^{\text{spin}}(\vec{r})$ is completely determined (i.e., gauge invariant). Earlier papers described a method for computing the root mean squared error (RMSE) between $V(\vec{r})$ and the electrostatic potential generated by a set of NACs in a way that automatically corrects for the arbitrary constant in $V(\vec{r})$.[16,54] We now describe a method for quantifying the accuracy of ASMs for reproducing $\vec{B}^{\text{spin}}(\vec{r})$. The accuracy of each ASM model for reproducing $\vec{B}^{\text{spin}}(\vec{r})$ was quantified by the mean absolute error (MAE):

$$
\text{MAE} = \sum_{\vec{p}}|(\vec{B}^{\text{spin}}(\vec{p})|_{\text{ASM}} - \vec{B}^{\text{spin}}(\vec{p})|_{\text{spindensity}})|u(\vec{p})/\sum_{\vec{p}}u(\vec{p})
\tag{24}
$$

where $\vec{B}^{\text{spin}}(\vec{p})|_{\text{ASM}}$ and $\vec{B}^{\text{spin}}(\vec{p})|_{\text{spindensity}}$ are the values at grid point $\vec{p}$ due to the ASM's and ab initio spin density, respectively. The finite element volume, $u(\vec{p})$, for each grid point makes the summations in eq 24 equivalent to corresponding integrals over volume. $\vec{B}^{\text{spin}}(\vec{p})|_{\text{spindensity}}$ was computed by numerically

integrating

$$
\vec{B}^{\text{spin}}(\vec{p}) = \frac{\mu_0}{4\pi}\left(\frac{g_e\mu_B}{2}\right)\oint\left(\frac{3(\vec{p} - \vec{r}')(\vec{m}(\vec{r}')\cdot(\vec{p} - \vec{r}'))}{|\vec{p} - \vec{r}'|^5} - \frac{\vec{m}(\vec{r}')}{|\vec{p} - \vec{r}'|^3}\right)\,\mathrm{d}^3\vec{r}'
\tag{25}
$$

We found that integrating $\vec{r}'$ over grid points inside the surface defined by $2.4\times$vdW radii enclosed essentially all of the spin density. (The vdW radii listed in the Supporting Information of Watanabe et al. were used.[16]) To avoid division by $|\vec{p} - \vec{r}'| = 0$ in eq 25, the set of grid points, $\{\vec{p}\}$, used to compute the MAE were distributed in the volume between surfaces defined by $3\times$ and $4\times$ vdW radii. The relative mean absolute error (RMAE) was then defined as the MAE for an ASM model divided by the MAE when all ASMs were set to zero.

2.2. New Optimization Functional for Computing ASMs. Now that general equations applicable to all AIM methods have been described in the previous section, we describe strategies for optimizing ASMs using AIM methods like DDEC that simultaneously optimize the $\rho_A(\vec{r}_A)$ distributions to be close to spherical symmetry and to resemble the electron distributions of isolated reference atoms.[14] To be chemically meaningful, the spin projected electron density $\rho_A(\vec{r}_A,\hat{h})$ must always be non-negative, which requires

$$
\kappa_A(\vec{r}_A) = \rho_A(\vec{r}_A) - m_A(\vec{r}_A) \geq 0
\tag{26}
$$

Equation 26 confines $m_A(\vec{r}_A)$ to the region of space where $\rho_A(\vec{r}_A)$ is non-negligible. Since DDEC $\rho_A(\vec{r}_A)$ distributions decay approximately exponentially with increasing r_A,[14] $m_A(\vec{r}_A)$ becomes negligible for sufficiently large r_A. In the remainder of this section, a suitable functional for optimizing $m_A(\vec{r}_A)$ subject to constraint 26 is derived.

One of the simplest optimization functionals would be to minimize the weighted sum of $|\vec{m}_A(\vec{r}_A) - \vec{m}_A^{\text{avg}}(r_A)|^2$ subject to constraints 11 and 26, which is denoted LSF (least-squares fitting) in the Results below. After programming this functional as described in the Supporting Information, we found that it performs poorly for dense systems containing adjacent magnetic atoms. For example, LSF requires 2094 iterations to converge the ASMs for solid Fe_3Si. Such a large number of iterations usually indicates a nearly flat optimization landscape. Nearly flat landscapes are problematic because the location of the minimum is unduly sensitive to small perturbations. As shown in the Results below, LSF gives the wrong sign for the ASM of Si in solid Fe_3Si. Earlier, we encountered analogous problems when $\rho_A(\vec{r}_A)$ was optimized to be as close to $\rho_A^{\text{avg}}(r_A)$ as possible.[14] In that case, the remedy was an optimization functional that minimizes the sum of $\rho_A(\vec{r}_A)\ln(\rho_A(\vec{r}_A)/w_A(r_A))$ where $w_A(r_A)$ is a weighted geometric average of a reference density and $\rho_A^{\text{avg}}(r_A)$ subject to the constraint that $w_A(r_A)$ does not become too diffuse.[14] A functional of this type minimizes the information distance between $\rho_A(\vec{r}_A)$ and $w_A(r_A)$ subject to the applied constraints. We found a similar strategy works for optimizing the atomic spin densities and reduces the number of iterations to approximately 10—a 2 orders of magnitude improvement. As shown in the Results below, this strategy gives accurate ASMs for solid Fe_3Si and other materials.

Specifically, we construct an optimization functional for the spin density projected onto the unit direction, $\hat{h}$, by minimizing the information distance $\rho_A(\vec{r}_A,\hat{h})\ln(\rho_A(\vec{r}_A,\hat{h})/w_A^{\text{spin}}(\vec{r}_A,\hat{h}))$ between $\rho_A(\vec{r}_A,\hat{h})$ and $w_A^{\text{spin}}(\vec{r}_A,\hat{h})$ subject to constraints 11 and 26. We found that excellent performance is obtained when

4149

dx.doi.org/10.1021/ct200539n |J. Chem. Theory Comput. 2011, 7, 4146–4164

$w_A^{spin}(\vec{r}_A, \hat{h})$ is a weighted geometric average between proportional spin partitioning and $\rho_A^{avg}(r_A, \hat{h})$

$$w_A^{spin}(\vec{r}_A, \hat{h}) = (\rho_A^0(\vec{r}_A, \hat{h}))^{\chi_{spin}} (\rho_A^{avg}(r_A, \hat{h}))^{1 - \chi_{spin}} \quad (27)$$

where proportional spin partitioning is defined by

$$\vec{m}_A^0(\vec{r}_A) = \vec{m}(\vec{r}) \rho_A(\vec{r}_A)/\rho(\vec{r}) \quad (28)$$

This has a form analogous to the weight used in DDEC charge partitioning.[14] Reasonable values of χ_{spin} are in the range $0 < \chi_{spin} \leq 1$. In the Results below, we study $\chi_{spin} = 3/14$ (~ 0.21), 0.5, and 1. $\chi_{spin} = 1$ gives proportional spin partitioning. To accommodate both collinear and noncollinear magnetism, integration is performed over all possible choices of $\hat{h}$. This gives the following optimization functional:

$$H = \sum_A \left(\oint_\omega \oint \rho_A(\vec{r}_A, \hat{h}) \ln\left(\frac{\rho_A(\vec{r}_A, \hat{h})}{w_A^{spin}(\vec{r}_A, \hat{h})}\right) d^3\vec{r}_A \, d^2\omega \right.$$
$$\left. - \oint \nu_A(\vec{r}_A) \kappa_A(\vec{r}_A) d^3\vec{r}_A \right) + \int_U \vec{\Lambda}(\vec{r}) \vec{\Delta}(\vec{r}) d^3\vec{r} \quad (29)$$

where the Lagrange multipliers $\nu(\vec{r}_A) \geq 0$ and $\vec{\Lambda}(\vec{r})$ are used to enforce constraints 26 and 11, respectively. Integration over ω means integration over all possible choices for $\hat{h}$, because ω is the unit sphere surface comprised of all possible end points for $\hat{h}$. Minimization occurs when

$$\delta H = \sum_A \oint \frac{\partial H}{\partial \vec{m}_A(\vec{r}_A)} \cdot \delta \vec{m}_A(\vec{r}_A) \, d^3\vec{r}_A = 0 \quad (30)$$

for arbitrary $\delta\vec{m}_A(\vec{r}_A)$, which is true when

$$\frac{\partial H}{\partial \vec{m}_A(\vec{r}_A)} = \frac{1}{2} \oint_\omega \ln\left(\frac{\rho_A(\vec{r}_A, \hat{h})}{w_A^{spin}(\vec{r}_A, \hat{h})}\right) \hat{h} \, d^2\omega - \vec{\Lambda}(\vec{r})$$
$$+ \nu_A(\vec{r}_A) \hat{m}_A(\vec{r}_A) \quad (31)$$

equals zero, where the vector partial derivative is defined as

$$\frac{\partial}{\partial \vec{b}} = \hat{x} \frac{\partial}{\partial b_x} + \hat{y} \frac{\partial}{\partial b_y} + \hat{z} \frac{\partial}{\partial b_z} \quad (32)$$

To evaluate the integral in eq 31, we first define the following function of $\vec{\tau}$ with $0 \leq \tau \leq 1$:

$$\xi(\tau)\hat{\tau} = \oint_\omega \ln(1 + \vec{\tau} \cdot \hat{h}) \hat{h} \, d^2\omega \quad (33)$$

By symmetry, the integral on the right-hand side must be parallel to $\hat{\tau}$. Without a loss of generality, we choose a set of spherical coordinates having $\hat{z} = \hat{\tau}$, and then rewrite eq 33 as

$$\xi(\tau) = \int_0^\pi \int_0^{2\pi} \cos(\phi) \ln(1 + \tau \cos(\phi)) \sin(\phi) \, d\theta \, d\phi \quad (34)$$

Analytic evaluation of this integral gives

$$\xi(\tau) = \pi\left((\tau^{-2} - 1) \ln\left(\frac{1 - \tau}{1 + \tau}\right) + \frac{2}{\tau}\right) \quad (35)$$

Note that $\xi(0) = 0$ and $\xi(1) = 2\pi$. After defining the functions

$$\vec{\vartheta}(a, \vec{b}) = \frac{\hat{b}}{2} \xi\left(\frac{b}{a}\right) \quad (36)$$

$$\vec{L}_A(\vec{r}_A) = \nu_A(\vec{r}_A) \hat{m}_A(\vec{r}_A) + \vec{\vartheta}(\rho_A(\vec{r}_A), \vec{m}_A(\vec{r}_A)) \quad (37)$$

$$\vec{\eta}_A(\vec{r}_A) = (1 - \chi_{spin}) \vec{\vartheta}(\rho_A^{avg}(r_A), \vec{m}_A^{avg}(r_A))$$
$$+ \chi_{spin} \vec{\vartheta}(\rho_A(\vec{r}_A), \vec{m}_A^0(\vec{r}_A)) \quad (38)$$

$$\vec{\Lambda}_A(\vec{r}_A) = \vec{L}_A(\vec{r}_A) - \vec{\eta}_A(\vec{r}_A) \quad (39)$$

equations 14, 31, 33, and 36−39 can be combined to give the solution of the optimization problem

$$\vec{\Lambda}_A(\vec{r}_A) = \vec{\Lambda}(\vec{r}) \quad (40)$$

A proof that $\{\vec{m}_A(r_A)\}$ are uniquely determined because H has only one minimum is given in the Appendix.

2.3. DFT Functionals for Noncollinear Magnetism. The accuracy of computed ASMs depends on the accuracy of the XC functional used to compute $\rho(\vec{r})$ and $\vec{m}(\vec{r})$. In noncollinear DFT, the total XC energy is formally a unique functional of the four spinor components at all positions in space:[25,35]

$$E_{XC}^{non\text{-}collinear} = E_{XC}^{four}(\{\rho(\vec{r}), \vec{m}(\vec{r})\}) \quad (41)$$

On the other hand, the total XC energy for collinear magnetism is formally a unique functional of two electron density components, $\rho^\alpha(\vec{r})$ and $\rho^\beta(\vec{r})$, at all positions in space:[25]

$$E_{XC}^{collinear}(\{\rho^\alpha(\vec{r}), \rho^\beta(\vec{r})\}) \quad (42)$$

All derivatives of the electron and spin densities are already included in functionals 41 and 42, because a function's derivatives are computed from values of that function at different positions. Density functionals originally developed for collinear magnetism are commonly extended to noncollinear magnetism by replacing $\rho^\alpha(\vec{r})$ and $\rho^\beta(\vec{r})$ in eq 42 with the spin densities projected onto the local spin magnetization direction:[25,35]

$$\rho^{(+)}(\vec{r}) = \rho(\vec{r}, +\hat{m}(\vec{r})) = (\rho(\vec{r}) + m(\vec{r}))/2 \quad (43)$$

$$\rho^{(-)}(\vec{r}) = \rho(\vec{r}, -\hat{m}(\vec{r})) = (\rho(\vec{r}) - m(\vec{r}))/2 \quad (44)$$

to give an XC functional that depends only on $\rho(\vec{r})$ and $m(\vec{r})$:

$$E_{XC}^{two}(\{\rho(\vec{r}), m(\vec{r})\}) \quad (45)$$

Functional 45, which can be conveniently applied to both collinear and noncollinear magnetism, is formally exact for collinear magnetism because it involves two spinor components. Local spin density approximations (LSDA) and generalized gradient approximations (GGA) are explicit analytic functionals of form 42 that can readily be converted to form 45 using eqs 43 and 44.

To quantify the inherent limitations of E_{XC}^{two} for modeling noncollinear magnetism, we consider its ability to reproduce the derivatives

$$\nu_{XC}(\vec{r}) = \frac{\partial E_{XC}}{\partial \rho(\vec{r})} \quad (46)$$

4150

dx.doi.org/10.1021/ct200539n | J. Chem. Theory Comput. 2011, 7, 4146−4164

$$\vec{B}_{\text{XC}}(\vec{r}) = \frac{\partial E_{\text{XC}}}{\partial \vec{m}(\vec{r})} \tag{47}$$

where $v_{\text{XC}}(\vec{r})$ and $\vec{B}_{\text{XC}}(\vec{r})$ are called the XC potential and XC magnetic field, respectively.[55,56] Inserting eq 45 into 47 and using the chain rule of differentiation gives

$$\vec{B}_{\text{XC}}^{\text{two}}(\vec{r}) = \frac{\partial m(\vec{r})}{\partial \vec{m}(\vec{r})} \frac{\partial E_{\text{XC}}^{\text{two}}(\{\rho(\vec{r}), m(\vec{r})\})}{\partial m(\vec{r})} \tag{48}$$

Since $\partial m(\vec{r})/\partial \vec{m}(\vec{r}) = \hat{m}(\vec{r})$, $\vec{B}_{\text{XC}}^{\text{two}}(\vec{r})$ is always parallel to $\hat{m}(\vec{r})$:

$$\vec{B}_{\text{XC}}^{\text{two}}(\vec{r}) = \hat{m}(\vec{r}) \, \partial E_{\text{XC}}^{\text{two}}(\{\rho(\vec{r}), m(\vec{r})\})/\partial m(\vec{r}) \tag{49}$$

Capelle et al. showed that the exact $\vec{B}_{\text{XC}}(\vec{r})$ is not parallel to $\vec{m}(\vec{r})$ if $\vec{\nabla} \cdot [J^{\text{KS}}(\vec{r}) - J(\vec{r})] \neq \vec{0}$, where $J^{\text{KS}}(\vec{r})$ and $J(\vec{r})$ are the spin-current tensors of the DFT noninteracting system and real interacting system, respectively.[55] Thus, eq 49 describes a fundamental limitation of all XC functionals that depend only on $\{\rho(\vec{r}), m(\vec{r})\}$. This limitation was previously reported for LSDA and GGA functionals.[55,56]

What is missing from $E_{\text{XC}}^{\text{two}}$ that forces $\vec{B}_{\text{XC}}^{\text{two}}(\vec{r})$ to be parallel to $\hat{m}(\vec{r})$? The functional $E_{\text{XC}}^{\text{two}}$ does not include any dependence on $\hat{m}(\vec{r})$. These directional changes can be quantified by the non-negative descriptors

$$f^{\text{dir}}(\vec{r}) = m(\vec{r})^2 \sum_{i=1}^{3} (\nabla_i \hat{m}(\vec{r}) \cdot \nabla_i \hat{m}(\vec{r})) \geq 0 \tag{50}$$

$$\Xi^{\text{dir}} = \int_{\tilde{U}} f^{\text{dir}}(\vec{r}) \, d^3\vec{r} \geq 0 \tag{51}$$

Analogous descriptors can be defined for the changes in $m(\vec{r})$

$$f^{\text{mag}}(\vec{r}) = \vec{\nabla} m(\vec{r}) \cdot \vec{\nabla} m(\vec{r}) \geq 0 \tag{52}$$

$$\Xi^{\text{mag}} = \int_{\tilde{U}} f^{\text{mag}}(\vec{r}) \, d^3\vec{r} \geq 0 \tag{53}$$

Non-negative measures of all gradient changes in $\vec{m}(\vec{r})$ are

$$f^{\text{tot}}(\vec{r}) = \sum_{i=1}^{3} (\nabla_i \vec{m}(\vec{r}) \cdot \nabla_i \vec{m}(\vec{r}))$$

$$= f^{\text{dir}}(\vec{r}) + f^{\text{mag}}(\vec{r}) \geq 0 \tag{54}$$

$$\Xi^{\text{tot}} = \Xi^{\text{mag}} + \Xi^{\text{dir}} \geq 0 \tag{55}$$

Clearly, $\Xi^{\text{tot}} = 0$ for nonmagnetic systems, and $\Xi^{\text{tot}} > 0$ for magnetic systems. Similarly, $\Xi^{\text{dir}} = 0$ for collinear magnetism, and $\Xi^{\text{dir}} > 0$ for noncollinear magnetism. Thus, it follows that

$$\lim_{\Xi^{\text{dir}} \to 0} E_{\text{XC}}^{\text{four}} = E_{\text{XC}}^{\text{two}} \tag{56}$$

In practice, we expect $E_{\text{XC}}^{\text{two}}$ to provide a reasonable approximation to the XC energy of a system's ground state when most of the $\vec{m}(\vec{r})$ changes are due to $m(\vec{r})$ changes, i.e., when $\Xi^{\text{dir}} \ll \Xi^{\text{mag}}$. For the ground states of many noncollinear magnetic materials, $\hat{m}(\vec{r})$ changes significantly only in regions where $m(\vec{r})$ is small,[22,57−59] leading to $\Xi^{\text{dir}} \ll \Xi^{\text{mag}}$ and $E_{\text{XC}}^{\text{non-collinear}} \approx E_{\text{XC}}^{\text{two}}$.

For example, consider the spin spiral ground state that has been experimentally observed in γ-Fe.[60] In this state, the ASMs exhibit a combined rotation-translation symmetry group.[59] $\hat{M}_A$ is significantly different for different Fe atoms, even though M_A is similar.[59] Furthermore, $\hat{m}(\vec{r})$ is approximately constant inside a

single atomic volume and changes only in regions of space where $m(\vec{r})$ is small.[59] From this, we infer $\Xi^{\text{dir}} \ll \Xi^{\text{mag}}$. Accordingly, computations showed $E_{\text{XC}}^{\text{two}}$ using the GGA approximation correctly reproduces the spin spiral ground state of γ-Fe for an appropriate range of lattice constants.[59] In summary, we derived the conditions under which the XC functional is accurately modeled by $E_{\text{XC}}^{\text{two}}$. This is used to apply the PW91 functional to noncollinear magnetism in section 4.3 below.

3. METHODS

3.1. Iterative Solution Algorithm for ASMs. We showed above that the task of assigning ASMs can be formulated in terms of optimizing the functional H defined in eq 29. We now describe an iterative algorithm that efficiently converges to H's unique minimum. Each iteration involves three loops. The first loop runs over $\{A, \vec{r}_A\}$, where all grid points having $r_A \leq r_{\text{cutoff}}$ are included. A cutoff of 4 Å was used in all calculations reported below. This loop generates an updated and unstored estimate of $\vec{m}_A(\vec{r}_A)$ that is used to accumulate sums stored for use in the second and third loops. In the first iteration, proportional partitioning is used:

$$\vec{m}_A(\vec{r}_A)|_1 = \vec{m}_A^0(\vec{r}_A) \tag{57}$$

$$\nu_A(\vec{r}_A)|_1 = 0 \tag{58}$$

For reasons that will be explained below, in subsequent iterations, an estimate for $\vec{L}_A(\vec{r}_A)$ is computed by

$$\vec{L}_A(\vec{r}_A) = \vec{Y}(\vec{r}) - \vec{\Omega}(\vec{r})$$

$$+ c \frac{(\vec{m}(\vec{r}) - \vec{m}^{\text{trial}}(\vec{r}))}{\rho(\vec{r})} + \vec{\eta}_A(\vec{r}_A) \tag{59}$$

The optimal value $c = \pi$ is derived in the Appendix. The magnitude $L_A(\vec{r}_A)$ was used to update the estimate for $m_A(\vec{r}_A)$ according to two cases. Case 1: if $L_A(\vec{r}_A) > \pi$, then $m_A(\vec{r}_A) = \rho_A(\vec{r}_A)$ and $\nu_A(\vec{r}_A) = L_A(\vec{r}_A) - \pi > 0$. Case 2: if $L_A(\vec{r}_A) \leq \pi$, $m_A(\vec{r}_A) = \rho_A(\vec{r}_A) \, \xi^{\text{inv}}(2L_A(\vec{r}_A))$ and $\nu_A(\vec{r}_A) = 0$, where the algorithm for computing ξ^{inv} is given in the Appendix. These two cases ensure that eq 26 is satisfied for all iterations and $\nu_A(\vec{r}_A) \geq 0$. The updated magnetization is given by

$$\vec{m}_A(\vec{r}_A) = m_A(\vec{r}_A)\hat{L}_A(\vec{r}_A) \tag{60}$$

During this loop, the sum of valid grid points for each r_A is accumulated and stored, as well as the accumulated sum of $\vec{m}_A(\vec{r}_A)$ for each r_A value. Finally, the following sums are also accumulated and stored

$$\vec{Y}(\vec{r}) = \sum_{k, A} \vec{L}_A(\vec{r}_A) \frac{\rho_A(\vec{r}_A)}{\rho(\vec{r})} \tag{61}$$

$$\vec{m}^{\text{trial}}(\vec{r}) = \sum_{k, A} \vec{m}_A(\vec{r}_A) \tag{62}$$

The second loop runs over $\{A, r_A\}$. This loop computes and stores $\vec{m}_A^{\text{avg}}(r_A)$, $m_A^{\text{avg}}(r_A)$, and M_A from the sums accumulated in the first loop. The third loop runs over $\{A, \vec{r}_A\}$ like the first loop. This loop accumulates and stores

$$\vec{\Omega}(\vec{r}) = \sum_{k, A} \left(\vec{\eta}_A(\vec{r}_A) \frac{\rho_A(\vec{r}_A)}{\rho(\vec{r})} \right) \tag{63}$$

After the third loop, the program starts the next iteration by going back to the first loop. At least five iterations were performed in all cases. Additional iterations were performed until all components in $\{M_A\}$ changed by less than 5×10^{-5}.

We now show this iterator robustly converges to H's global minimum. Upon convergence, multiplying eq 59 by $\rho_A(\vec{r}_A)/\rho(\vec{r})$ and summing over $\{k_1, k_2, k_3, A\}$ gives

$$\vec{0} = c(\vec{m}(\vec{r}) - \vec{m}^{\text{trial}}(\vec{r}))/\rho(\vec{r}) \tag{64}$$

which proves constraint 11 is satisfied. Therefore, at convergence, eq 59 gives

$$\vec{\Lambda}_A(\vec{r}_A) = \vec{L}_A(\vec{r}_A) - \vec{\eta}_A(\vec{r}_A) = \vec{Y}(\vec{r}) - \vec{\Omega}(\vec{r}) = \vec{\Lambda}(\vec{r}) \tag{65}$$

which is the required solution. The iterative scheme converges $\vec{\Lambda}_A(\vec{r}_A)$ to a function $\vec{\Lambda}(\vec{r})$ that is the same for all atoms using an averaging mechanism. Specifically, in each iteration, the updated estimate for the function $\vec{\Lambda}(\vec{r}) = \vec{Y}(\vec{r}) - \vec{\Omega}(\vec{r})$ is constructed by averaging the $\vec{\Lambda}_A(\vec{r}_A)$ values over all atoms. Using eq 59, this $\vec{\Lambda}(\vec{r})$ estimate is used in the subsequent iteration to compute a new estimate for $\vec{\Lambda}_A(\vec{r}_A)$. This causes the estimated $\vec{\Lambda}_A(\vec{r}_A)$ for all atoms to rapidly converge toward an average value, $\vec{\Lambda}(\vec{r})$, thereby solving the optimization problem. When using $\chi_{\text{spin}} = 1/2$ or 3/14, we have not encountered any system for which more than 10 and 20 iterations, respectively, were required to converge $\{M_A\}$ to within 5×10^{-5}.

Our implementation is computationally efficient. For materials containing several hundred atoms, a large amount of memory would be required to store the complete set of functions of $\vec{r}_A$. The above approach minimizes overall memory requirements by only requiring functions of $\vec{r}_A$ to be stored for the current position. This allows systems containing hundreds of atoms in the unit cell to be analyzed on a typical computer processor with a few gigabytes of memory. Since only complete functions of $\vec{r}$ and r_A need to be stored, the overall memory requirements scale linearly with the number of grid points (i.e., volume) in the unit cell. The use of a cutoff radius causes the overall computational time to scale linearly with the number of atoms in the unit cell. In summary, both the computational time and the memory requirements scale linearly with increasing system size, which makes the algorithm efficient for both small and large systems. These same properties hold for the DDEC charge analysis.[14] For collinear magnetism, all $\vec{m}_A(\vec{r}_A)$ are parallel to a global magnetization axis. In this case, vectors can be replaced with their scalar projection onto the global magnetization axis. It is therefore only necessary to compute and store one-third as many components as in the noncollinear case. For collinear magnetism, our implementation automatically avoids the computation and storage of all zero-valued spin components. Except for this simplification, all other details are the same for the collinear and noncollinear cases.

3.2. Geometry and Electron Density Generation. All periodic DFT calculations were performed in the Vienna Ab Initio Simulation Package (VASP)[61,62] using the projector augmented wave (PAW) method[63] and a 400 eV cutoff. For all periodic systems, the product of the number of k points and the unit cell volume exceeded 4000 Å^3, except for the HSE06 calculation of magnetite, which was performed only at the Γ point. All nonperiodic calculations were performed using Gaussian software.[64] The XC functionals, basis sets, and additional details are described in the Results section below. The PW91-optimized geometry[65] for the $Cu_3(BTC)_2$ metal organic framework (MOF) and experimental Fe_3Si crystal geometry[66] were taken from the literature. The remaining geometries were optimized in VASP or Gaussian. In VASP, geometries were optimized to give atomic forces <0.03 eV/Å. In Gaussian, geometries were optimized to give atomic forces and displacements smaller than 0.0025 au and 0.01 au, respectively.

Core−valence XC interactions are critical for describing the properties of magnetic materials.[67] The PAW method has many advantages, especially for studying magnetic materials, because it is an all-electron frozen core method that explicitly includes core−valence XC interactions.[63] The PAW method has higher accuracy and similar computational cost to pseudopotential methods;[63] however, pseudopotentials that use partial core corrections to describe valence−core XC interactions can also give accurate results including magnetic properties.[67] For calculations employing linear combination of atomic orbital (LCAO) basis sets, relativistic effective core potentials (RECPs) that include outer-core shell electrons in the valence space can give accurate magnetic properties because they describe the most important valence−core XC interactions.[68] This is more important for s-, d-, and f-block elements than for p-block elements.[67,68] We used the PAW method for all periodic calculations in this paper. For nonperiodic calculations, we used all-electron basis sets on lighter atoms and appropriate RECPs for heavier atoms. The specific basis sets are listed in the Results below.

DDEC atomic charge distributions were computed using the DDEC/c2 method of Manz and Sholl.[14] Spherical averaging was performed using 75 radial shells evenly spaced between $r_A = 0$ and the cutoff radius of 4 Å. To make sure all electrons were included, core electrons replaced by a pseudopotential or effective core potential during a quantum chemistry calculation were automatically reinserted by the program at the beginning of DDEC analysis. (The program stores core electron reference densities for all chemical elements.) The speed of core charge fitting was improved by applying the constraint

$$w_A^{\text{core}}(r_A) = \min(\rho_A^{\text{core}}(r_A), \rho_A^{\text{core}}(r_A - \Delta r_A) \, e^{-2\Delta r_A/\text{bohr}}) \tag{66}$$

which ensured that $-d \ln(w_A^{\text{core}}(r_A))/dr_A \geq 2/\text{bohr}$, where Δr_A is the distance between adjacent radial shells. The core electron distributions of all isolated atoms naturally satisfy this constraint, because francium contains the most diffuse core electrons of all elements with a decay exponent of 2.14/bohr. This reduced the number of core fitting iterations to less than 30 (from an initial value of ∼200 in some cases) with no significant effect on the resulting atomic charges.

Three radial shell and cutoff radius combinations are currently available in the program at ddec.sourceforge.net: (a) 50 radial shells with a 3 Å cutoff, (b) 75 radial shells with a 4 Å cutoff, and (c) 100 radial shells with a 5 Å cutoff. Examining the c2 reference densities[14] for different elements in the periodic table shows that 75 radial shells with a 4 Å cutoff is a good choice for nearly all chemical systems. Specifically, the most diffuse neutral atoms with atomic numbers ≤ 109 are francium and radium, which have 0.11 electrons between 4 and 5 Å. Commonly, Fr is in the +1 charge state, where it has only 0.0002 electrons between 4 and 5 Å. The O^{2-} and Te^{2-} anions (which are among the most diffuse of the commonly occurring anions) have 0.003 and 0.028 electrons between 4 and 5 Å, respectively. Ions like Cr^- and Mo^- are more diffuse with 0.048 and 0.053 electrons between 4 and 5

4152

dx.doi.org/10.1021/ct200539n |J. Chem. Theory Comput. 2011, 7, 4146–4164

Å, respectively; however, these anions are not commonly occurring. Thus, a 4 Å cutoff is sufficient to converge the NACs and ASMs to within approximately ±0.01 electrons for almost all chemical systems. A 5 Å cutoff is available for cases containing extremely diffuse atoms. For a given unit cell, the time required to compute NACs and ASMs scales linearly with the number of grid points per atom which in turn scales linearly with the cube of the cutoff radius. Consequently, using a 4 Å cutoff takes about twice as long as a 3 Å cutoff and about half as long as a 5 Å cutoff. Tests were performed for χ_{spin} = 1/2 using TiI placed in the center of a $10 \times 10 \times 10$ Å super cell. For different cutoff values, the ratio of times to compute NACs was time(3 Å)/time(4 Å) = 0.47 and time(5 Å)/time(4 Å) = 1.72, and that to compute ASMs was time(3 Å)/time(4 Å) = 0.43 and time(5 Å)/time(4 Å) = 1.77. NACs differed by ±0.01 (5 Å) and ±0.05 (3 Å) relative to the 4 Å values. The iodine ASM changed by less than 0.002 when the cutoff radius was changed. The Ti ASM decreased from 3.076 (5 Å) to 3.066 (4 Å) to 3.001 (3 Å). The total spin moment was 2.930 (3 Å), 2.990 (4 Å), and 2.999 (5 Å) compared to the exact value of 3, which shows that about 0.07 and 0.01 polarized electrons were missed by the 3 and 4 Å cutoffs, respectively. For all of the other iodides in the Results below, <0.01 polarized electrons were missed by the 4 Å cutoff.

Bader atomic volumes were computed by the program of Henkelman and co-workers using the total electron density; then the valence and spin densities were integrated over these volumes to determine the atomic charges and ASMs, respectively.[69−71] Bader's method can sometimes yield compartments that do not include an atomic nucleus (i.e., non-nuclear attractors).[72] For the all-electron calculations studied in this paper, the number of Bader compartments was the same as the number of atoms, and there were no non-nuclear attractors. For calculations with RECPs (i.e., LANL2DZ and SDD basis sets), the core electron density replaced by the RECP was not included in the Bader analysis, and this resulted in non-nuclear maxima and several compartments per atom. We found that reliable Bader NACs and ASMs were obtained by assigning each compartment to the nearest nucleus, as done in the program of Henkelman and co-workers.[69−71] In both Bader and DDEC analysis, the typical mesh size was ∼0.05 Å, which provided <0.1 error in the total number of valence electrons. The valence electron density was then rescaled to provide the exact number of valence electrons. Natural population analysis was performed using the NBO 3.0 program[73] within Gaussian. Integration of the total spin density within an effective atomic sphere radius was performed using the Lorbit method in VASP using the default radii.

Attempts to compute Mulliken populations projected onto a minimal basis set (MBS) had limited success. As currently implemented in Gaussian 09, MBS population analysis projects onto a STO-3G basis set, which is only defined for atomic numbers ≤ 53.[15,64] Consequently, MBS analysis could not be performed for $[GdI]^{2+}$. The MBS method also requires the basis set used to compute the SCF wave function to be larger than the STO-3G basis set. This can become a critical problem when a RECP is used, since in this case the basis set used to compute the SCF wave function only needs to model valence electrons while the STO-3G basis set is all-electron. Consequently, MBS analysis could not be performed for MgI, MoI, SnI, or TeI when using SDD basis sets (which includes RECPs). It may be possible to fix some of these issues by treating valence and core electrons separately and projecting onto a different basis set than STO-3G. We were able to perform MBS analysis for TiI, the Cu_2
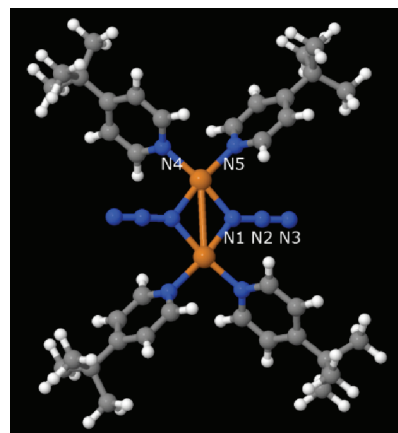

Figure 1. Cu_2 organometallic complex with triplet ground state and +2 net charge (atoms: Cu (gold), N (blue), C (gray), H(white)).

organometallic complex shown in Figure 1, and $[Cr(CN)_6]^{3-}$. For TiI using SDD basis sets, the MBS NACs were 0.26 (Ti) and −0.26 (I), and the MBS ASMs were 3.14 (Ti) and −0.26 (I), which are reasonable. For the complex in Figure 1, the MBS NACs were 0.50 (Cu), −0.30 to 0.06 (C atoms), 0.09 to 0.16 (H atoms), and −0.33 to 0.15 (N atoms), and the MBS ASMs were 0.61 (Cu), −0.01 to 0.01 (C atoms), 0.00 (H atoms), and −0.03 to 0.13 (N atoms), which are reasonable. For $[Cr(CN)_6]^{3-}$ with 6-311+G* basis sets, the MBS NACs were −11.97 (Cr), −2.45 (four C's), −1.96 (two C's), 4.12 (four N's), and 4.11 (two N's), and the MBS ASM's were 0.02 (Cr), 0.69 (four C's), 0.20 (two C's), −0.04 (four N's), and −0.02 (two N's), which are unreasonable. Because of these difficulties, we do not consider MBS population analysis further in this paper.

For systems with collinear magnetism, noncollinear DFT calculations and ASM analysis should yield the same results as collinear DFT calculations and ASM analysis. As an example, we compared noncollinear vs collinear DFT calculations and ASM analysis for a MgI molecule placed in the center of a 10 Å × 10 Å × 10 Å super cell. Periodic DFT calculations were performed in VASP using the PBE XC functional.[74] The optimized collinear and noncollinear energies differed by less than 1 meV. Both collinear and noncollinear DFT calculations gave an optimized M = 1.000. For each of the χ_{spin}= 1.0, 3/14, and 1/2, and LSF methods, the ASM magnitudes computed with noncollinear analysis differed by <0.001 from those computed using collinear analysis. These results confirm noncollinear and collinear analysis yield essentially identical results for a system with collinear magnetism.

4. RESULTS AND DISCUSSION

4.1. Diatomic Iodides. We first consider a series of diatomic iodides XI {X = Mg, Ti, Mo, Sn, Te, Gd^{2+}} containing unpaired electrons. We specifically chose elements with electronegativity lower than iodine, so that one electron would be transferred to fill iodine's valence shell. Consequently, nearly all of the unpaired electrons reside on the X atom. This allows us to assess the accuracy of different ASM methods. Second, we computed the relative mean absolute error (RMAE) for fitting the magnetic field $\vec{B}^{spin}(\vec{r})$ in the volume between the surfaces defined by 3× and 4× vdW radii. Thus, the simplicity of these diatomic iodides allows us to objectively assess the accuracy of different ASM

Table 1. Atomic Spin Analysis of Diatomic Iodides

	total spin		atomic spin moment on cation												
			nonperiodic system[a]							periodic system[b]					
						χ_{spin}							χ_{spin}		
	other[c]	Lorbit[d]	Δ_S	Bader	NPA	1.0	3/14	1/2	LSF	Bader	Lorbit	1.0	3/14	1/2	LSF
MgI	1	0.23	0.00	0.85	0.87	0.85	0.99	0.93	1.04	0.85	0.14	0.85	1.02	0.94	1.06
TiI	3	2.26	0.02	3.03	3.13	3.01	3.25	3.14	3.29	2.96	2.29	2.93	3.17	3.07	3.22
MoI	5	4.00	0.03	4.95	5.00	4.87	5.12	5.01	5.17	4.89	4.00	4.82	5.09	4.97	5.13
SnI	1	0.54	0.00	0.94	1.00	0.94	1.03	0.99	1.06	0.94	0.52	0.92	1.02	0.98	1.05
TeI	1	0.52	0.00	0.85	0.87	0.84	0.88	0.86	0.89	0.81	0.41	0.80	0.84	0.82	0.86
$[GdI]^{2+}$	7	6.88	0.45	6.64	6.60	6.65	6.63	6.64	6.63	6.93	6.85	6.92	6.94	6.93	6.94

| | | RMAE for the nonperiodic system [relative rank in brackets] | | | | | | |
	zero ASM MAE (gauss)[e]	Bader	Lorbit	NPA	$\chi_{spin} = 1.0$	$\chi_{spin} = 3/14$	$\chi_{spin} = 1/2$	LSF
MgI	32	0.249 [5]	0.813 [7]	0.237 [4]	0.249 [5]	0.174 [2]	0.201 [3]	0.161 [1]
TiI	88	0.050 [5]	0.257 [7]	0.038 [3]	0.053 [6]	0.034 [1]	0.037 [2]	0.041 [4]
MoI	144	0.027 [5]	0.204 [7]	0.021 [4]	0.038 [6]	0.010 [1]	0.020 [3]	0.014 [2]
SnI	22	0.085 [5]	0.472 [7]	0.060 [2]	0.085 [5]	0.059 [1]	0.063 [3]	0.068 [4]
TeI	21	0.043 [5]	0.491 [7]	0.038 [2]	0.047 [6]	0.037 [1]	0.040 [4]	0.039 [3]
$[GdI]^{2+}$	194	0.0038 [1]	0.0340 [7]	0.0052 [6]	0.0040 [5]	0.0039 [3]	0.0038 [1]	0.0039 [3]
avg.		[4.3]	[7.0]	[3.5]	[5.5]	[1.5]	[2.7]	[2.8]
st. dev.		[1.6]	[0.0]	[1.5]	[0.5]	[0.8]	[1.0]	[1.2]
mean abs difference between cation ASM and total spin moment		0.13	0.63	0.13	0.14	0.15	0.12	0.17

[a] Nonperiodic system using SDD basis sets. [b] Periodic system using 10 Å × 10 Å × 10 Å cubic unit cell and PAW method. [c] Total spin of the molecule and sum of ASMs for all methods except Lorbit. [d] Sum of ASMs for the Lorbit method. [e] 1 gauss = 10^{-4} tesla.

methods for simultaneously fitting $\vec{B}^{spin}(\vec{r})$ and atomic chemical states.

Table 1 shows results computed with the PBE functional. For the nonperiodic calculations, SDD basis sets were used that included RECPs for I (46 core), Ti (10 core), Mo (28 core), Sn (46 core), Te (46 core), and Gd (28 core). Comparison is made to periodic calculations using the PAW method with a 10 Å × 10 Å × 10 Å super cell. Since iodine is not very magnetic, the cation ASM should be within ∼±0.2 of the total spin. The Bader; NPA; LSF; and χ_{spin}= 1, 3/14, and 1/2 methods gave ASMs in this expected range for all materials in Table 1 except when SDD basis sets were used for $[GdI]^{2+}$. Only for $[GdI]^{2+}$ were the SDD and PAW results significantly different, with PAW giving the expected moment and SDD giving a moment ∼0.35 different than expected. Consistent with these findings, Δ_S for SDD basis sets showed significant spin contamination (Δ_S = 0.45) for $[GdI]^{2+}$, and negligible spin contamination ($\Delta_S \leq 0.03$) for the other materials. ASMs computed by integrating the total spin density within an effective atomic sphere radius (denoted Lorbit) performed poorly because regions between the atomic spheres were not assigned to any atom, so the ASMs do not sum to the

total spin moment of the unit cell. For example, the sum of Lorbit ASMs for MgI was 0.23 compared to the correct value of 1. Table 1 also shows the relative rank of each method as defined by the computed RMAE values. The Lorbit method had a rank of 7 for each material, meaning it always gave the least accurate results among the seven ASM methods. Therefore, we do not consider Lorbit ASMs further in this paper.

Since decreasing the χ_{spin} value increases the proportion of spherical averaging in the optimization functional, smaller χ_{spin} values gave an improved prediction of $\vec{B}^{spin}(\vec{r})$, as evidenced by the smaller RMAE values. Among the seven ASM methods tested, using $\chi_{spin} = 3/14$ gave the most accurate prediction of $\vec{B}^{spin}(\vec{r})$. The $\chi_{spin} = 1/2$ and LSF methods were the next most accurate at predicting $\vec{B}^{spin}(\vec{r})$. Since RMAE is defined as the ratio of the mean absolute error (MAE) of the ASM model to the MAE when all ASMs were set to zero, the product of the RMAE and the zero ASM MAE recovers the computed MAE for each method. For example, the RMAE of MoI for the $\chi_{spin} = 1/2$ method was 0.020, and the zero ASM MAE was 144 gauss. The MAE computed from eq 24 was 0.020 × 144 gauss = 2.88 gauss for MoI using $\chi_{spin} = 1/2$. In other words, ASMs computed using

4154

dx.doi.org/10.1021/ct200539n |*J. Chem. Theory Comput.* 2011, 7, 4146–4164

Table 2. Atomic Charge Analysis of Diatomic Iodides

	optimized	net atomic charge on cation		
	d_0 (Å)	Bader	NPA	DDEC
MgI	2.69^a $[2.61]^b$	0.68^a $[0.76]^b$	0.61^a	0.41^a $[0.42]^b$
TiI	2.61^a $[2.61]^b$	0.51^a $[0.58]^b$	0.40^a	0.32^a $[0.37]^b$
MoI	2.67^a $[2.62]^b$	0.63^a $[0.60]^b$	0.39^a	0.32^a $[0.34]^b$
SnI	2.85^a $[2.74]^b$	0.26^a $[0.29]^b$	0.39^a	0.26^a $[0.23]^b$
TeI	2.80^a $[2.69]^b$	0.11^a $[0.02]^b$	0.06^a	0.02^a $[0.00]^b$
$[GdI]^{2+}$	2.73^a $[2.68]^b$	1.82^a $[1.66]^b$	1.86^a	1.91^a $[2.05]^b$
	RMSE no NACs (kcal/mol)	RRMSE for the nonperiodic system		
MgI	11.8	0.81	0.64	0.22
TiI	12.8	0.52	0.44	0.47
MoI	11.5	0.80	0.35	0.35
SnI	6.3	0.43	0.81	0.43
TeI	2.6	1.22	0.99	0.96
$[GdI]^{2+}$	41.5	0.13	0.15	0.17
avg.	14.4	0.65	0.56	0.43
st. dev.	13.8	0.38	0.31	0.28

^{a} Nonperiodic system using SDD basis sets. ^{b} Periodic system using 10 Å × 10 Å × 10 Å cubic unit cell and PAW method.

χ_{spin} = 1/2 predicted $\vec{B}^{spin}(\vec{r})$ 50 times more accurately than when ASMs for all atoms were set to zero. The accuracy of the methods for reproducing chemical states can be estimated by considering iodine to be an essentially nonmagnetic atom, which means the cation ASM should be close to the total spin moment. Among the seven ASM methods, using χ_{spin} = 1/2 gave the smallest mean absolute difference between the cation ASM and the total spin moment, suggesting that its accuracy is high. The Bader and NPA methods gave the next lowest values, suggesting they also have high accuracy. As shown in the rest of this paper, for most materials, the χ_{spin} = 1/2, Bader, and (where applicable) NPA methods give similar ASMs. Overall, these results suggest that using χ_{spin} = 1/2 gives an excellent combination of accuracy for reproducing both $\vec{B}^{spin}(\vec{r})$ and the chemical states of atoms in a material. This finding is encouraging, because the optimization functional in eq 29 is designed explicitly for this dual purpose.

Table 2 compares the Bader, NPA, and DDEC NACs for these same materials. When DDEC ASMs are computed using χ_{spin} = 1/2 as discussed above, the variation in NACs between Bader, NPA, and DDEC methods is larger than the variation in ASMs between these methods. This agrees with previous findings that NACs are more sensitive to the choice of population analysis method than ASMs are.[50] Table 2 also lists the relative root mean squared error (RRMSE) in $V(\vec{r})$ for each of the point charge models. RRMSE is defined as the root mean squared error (RMSE) of $V(\vec{r})$ for a point charge model divided by the RMSE when all NACs are set to zero, where grid points for computing RMSE are uniformly distributed between the surfaces defined by 1.4× and 2.0× vdW radii.[16,54,75] The RRMSE values in Table 2 suggest that the DDEC method is the most accurate for reproducing $V(\vec{r})$, which agrees with our previous findings.[14]

4.2. Comparison to Experimental Atomic Spin Moments. We now compare theoretically computed ASMs to experimental data for several molecules and crystals. Table 3 compares experimental[76−78] and computed ASMs for the Cu$_2$ organometallic complex shown in Figure 1, $[Cr(CN)_6]^{3−}$, and solid Fe$_3$Si.

Geometry optimization was performed for both the singlet and triplet states of the Cu$_2$ complex shown in Figure 1. The minimum energy singlet state was a closed shell singlet (all ASMs were zero) with an energy 0.78 eV above the minimum energy triplet state. This agrees with experiments showing that the ground state is a triplet.[76] Solid Fe$_3$Si has adjacent magnetic atoms with overlapping electron distributions. As mentioned above, the LSF method performs poorly for this type of material; specifically, LSF predicts the wrong sign for the ASM of Si and takes 2094 iterations to converge. For all three materials, the Bader and DDEC ASMs are close to each other and in good agreement with experiments. The value of χ_{spin} had a small effect on the computed ASMs but a large effect on the number of required iterations. For the two molecular systems, the small amount of spin contamination, $\Delta_S \leq$ 0.03, shows that DFT accurately reproduced the spin states. For these two systems, the NPA ASMs were similar to those of the other population analysis methods. NACs for all three materials are listed in the Supporting Information. For $[Cr(CN)_6]^{3−}$, the Cr NAC was 1.45 (Bader), 0.28 (DDEC), and −0.78 (NPA), which clearly shows that NACs are more sensitive than ASMs to the choice of population analysis method. The RMSE values for $[Cr(CN)_6]^{3−}$ were 1.3 (DDEC), 2.2 (NPA), 9.0 (Bader), and 16.9 (no charges) kcal/mol, which shows that DDEC was the most accurate for reproducing $V(\vec{r})$.

We now consider the computation of ASMs for a highly correlated material. Magnetite, which has an inverse spinel structure, has one tetrahedrally coordinated Fe atom and two octahedrally coordinated Fe atoms per formula unit.[79] The Fe(tet) atom has a formal oxidation state of +3. There are two possibilities for the Fe(oct). The first possibility is for the two Fe(oct) to be equivalent with a formal oxidation state of +2.5, and the second possibility is for one Fe(oct) to have a +2 oxidation state with the other having a +3 oxidation state.[79] Bulk magnetite undergoes a structural and electronic transition near T_V = 120 K called the Verwey transition,[80] whose precise mechanism is still debated.[81,82] Above T_V, electrons move rapidly between Fe(oct)s, causing them to appear equivalent with an effective +2.5 oxidation state. Progress has been made to use the ferrimagnetic half-metallic state of bulk magnetite above T_V for spintronics applications.[83−86] The redox properties of magnetite surfaces lead to unusual adsorption properties,[87,88] and a Verwey-like charge-spin ordering transition accompanies the magnetite (001) surface reconstruction.[89,90] Below T_V, the Fe(oct)s, in bulk magnetite become inequivalent and the crystal structure changes. As previously reported, the Hubbard on-site parameter U_{eff} offers a convenient way to artificially transition between these two regimes, because in a DFT +U calculation the Fe(oct) sites appear equivalent for $U_{eff} < 2.6$ eV but inequivalent for $U_{eff} > 2.6$ eV.[79] Table 4 shows the effect of the Hubbard on-site parameter on bulk magnetite's charge and spin ordering, using the PBE functional[74] and Dudarev et al.'s[91] DFT +U method. The lattice constant was optimized for each U_{eff} value using a cubic Fe$_6$O$_8$ unit cell, which is the experimental unit cell shape above T_V. As apparent from the NACs and ASMs shown in Table 4, the two Fe(oct) sites were equivalent for U_{eff} = 0 and inequivalent for U_{eff} = 3.2 eV. For U_{eff} = 3.2 eV, this also causes the O atoms to segregate into two groups with slightly different Fe−O distances (not shown), NACs, and ASMs. For U_{eff} = 3.2 eV, the Fe^{III}(tet) and Fe^{III}(oct) had the same Bader ($\sim$1.6) or DDEC ($\sim$2.0) NACs, which rationalizes an assignment of +3 oxidation for both sites. The experimental value for the Fe(tet) ASM is −3.82.[92] Irrespective of the population analysis method, our computations gave Fe(tet) ASM values slightly lower than this

4155

dx.doi.org/10.1021/ct200539n |J. Chem. Theory Comput. 2011, 7, 4146–4164

Table 3. Comparison of Calculated and Experimental Atomic Spin Moments

	exp. value	NPA	Bader	$\chi_{spin} = 1.0$	$\chi_{spin} = 3/14$	$\chi_{spin} = 1/2$	LSF
			Fe₃Si solid (PBE functional, optimized spin moment per unit cell =5.09)				
Fe	2.20[b]	n.a.	2.60	2.50	2.54	2.52	2.25
Fe	1.35[b]	n.a.	1.31	1.31	1.31	1.31	1.27
Fe	1.35[b]	n.a.	1.31	1.31	1.31	1.31	1.27
Si	−0.07[b]	n.a.	−0.14	−0.04	−0.07	−0.06	0.30
iterations[a]				1	17	7	2094
			$[Cr(CN)_6]^{3-}$ (B3LYP/6-311+G*, total spin moment = 3, Δ_S = 0.03)				
Cr	3.25[c]	2.96	2.85	2.81	2.97	2.90	3.10
C	−0.09[c]	−0.06	−0.03	−0.02	−0.06	−0.04	−0.10
N	0.05[c]	0.07	0.06	0.05	0.06	0.06	0.08
iterations[a]				1	17	9	66
			Cu₂ organometallic complex (B3LYP/LANL2DZ, total spin moment = 2, Δ_S = 0.01)				
Cu	0.77[d]	0.53	0.59	0.59	0.58	0.59	0.56
N1	0.07[d]	0.14	0.11	0.11	0.12	0.11	0.13
N2	−0.02[d]	−0.04	−0.02	−0.01	−0.03	−0.02	−0.04
N3	0.05[d]	0.13	0.12	0.11	0.13	0.12	0.13
N4	0.07[d]	0.12	0.10	0.09	0.10	0.09	0.12
N5	0.05[d]	0.12	0.10	0.09	0.10	0.09	0.12
other atoms	≤0.03[d]	≤0.01	<0.01	<0.01	<0.01	<0.01	<0.02
iterations[a]				1	12	7	64

[a] Iterations required to converge ASMs to within 5×10^{-5}. [b] From ref 78. [c] From ref 77. [d] From ref 76.

Table 4. Effect of XC Functional on Bulk Magnetite's Charge and Spin Ordering

			NAC		ASM				
	oxidation state	number per unit cell	Bader	DDEC	Bader	$\chi_{spin} = 1.0$	$\chi_{spin} = 3/14$	$\chi_{spin} = 1/2$	LSF
				U_{eff} = 0 (optimized lattice constant = 8.303 Å)					
Fe(oct)	2.5	4	1.46	1.53	3.56	3.43	3.52	3.49	3.33
Fe(tet)	3	2	1.46	1.74	−3.48	−3.32	−3.49	−3.42	−3.66
O	−2	8	−1.09	−1.20	0.09	0.12	0.11	0.11	0.25
iterations[a]						1	17	8	1130
				U_{eff} = 3.2 eV (optimized lattice constant = 8.435 Å)					
Fe(oct)	3	2	1.62	1.97	4.06	3.90	4.01	3.96	3.96
Fe(oct)	2	2	1.40	1.47	3.65	3.52	3.61	3.57	3.60
Fe(tet)	3	2	1.59	1.99	−3.98	−3.81	−4.00	−3.91	−4.10
O	−2	4	−1.15	−1.38	0.10	0.13	0.12	0.12	0.17
O	−2	4	−1.16	−1.34	0.04	0.07	0.06	0.06	0.09
iterations[a]						1	17	8	322
				HSE06 (optimized lattice constant = 8.35 Å)					
Fe(oct)	>2.5	2	1.66	1.89	3.96	3.82	3.93	3.88	3.87
Fe(oct)	<2.5	2	1.63	1.84	3.91	3.77	3.87	3.83	3.85
Fe(tet)	3	2	1.68	2.11	−4.02	−3.84	−4.02	−3.94	−4.12
O	−2	4	−1.23	−1.45	0.02	0.04	0.04	0.04	0.09
O	−2	4	−1.25	−1.47	0.06	0.08	0.07	0.08	0.11
iterations[a]						1	15	8	555

[a] Iterations required to converge ASMs to within 5×10^{-5}.

for U_{eff} = 0. On the other hand, for U_{eff} = 3.2 eV, the computed Fe(tet) ASM was equal to or slightly greater than the experimental value, which suggests that $0 < U_{eff} < 3.2$ eV is probably optimal for the description of charge and spin ordering in bulk magnetite. For both U_{eff} = 0 and 3.2 eV, the total spin moment per Fe₃O₄ formula unit was +4, and recent experiments gave approximately the same value.[93] The main conclusion from these results is that for highly correlated materials the XC theory has a

4156

dx.doi.org/10.1021/ct200539n |*J. Chem. Theory Comput.* 2011, 7, 4146–4164

larger effect on the computed ASMs than the population analysis method does.

These results reflect the tendency of common GGA functionals to overly delocalize electrons in many extended materials.[94,95] Specifically, the exact XC functional should vary linearly in the total number of electrons when the total number of electrons is fractional.[96] XC functionals giving convex behavior overly delocalize electrons in extended systems, while those giving concave behavior overly localize electrons in extended systems.[97] DFT+U is one method for approximately correcting delocalization errors.[98] Because $U_{eff} \gg 0$ favors the localization of electrons,[99] combining a functional like PBE or PW91 with a suitably chosen U_{eff} value can approximately cancel the delocalization error. The U_{eff} value can be different for different oxidation states and environments of the same element.[99] In the DFT+U example above, $U_{eff} = 3.2$ eV applies only to the Fe atoms, and $U_{eff} = 0$ for the oxygen atoms. The Hartree−Fock method has concave behavior, leading to overly localized electrons.[97] Thus, using a fraction of Hartree−Fock exchange to create a hybrid functional is another way to partially correct the delocalization error.[95,98,100] For range-separated hybrids, the fraction of HF exchange varies as a function of interelectron distance. The range-separated hybrid HSE06 improves performance in extended systems by mixing 75% PBE with 25% HF exchange at short interelectron distances and by using PBE alone at large interelectron distances.[101] For extended systems with conducting electrons, this has a lower computational cost and improved convergence with respect to k-point sampling than using the same fraction of HF exchange at all interelectron distances.[102,103] The NACs and ASMs for magnetite computed with HSE06 are shown in Table 4. Due to the higher computational cost associated with including HF exchange, this HSE06 calculation was performed only at the Γ point. As evident from the higher magnitude Fe ASMs in Table 4, the spin density is more localized for HSE06 than for PBE. The magnitude of the NACs is also higher for HSE06 than for PBE. The amount of charge and spin disproportionation between the different types of Fe(oct) sites is higher for PBE+U than for HSE06. For HSE06, the amount of charge disproportionation was <0.1 electron, while for PBE+U it was several tenths of an electron. The magnitude of the oxygen NAC was higher for HSE06 than for PBE+U. In summary, these results show that DFT+U and HSE06 increased the localization of charge and spin compared to PBE for the Fe atoms in magnetite.

4.3. A Single Molecule Magnet with Highly Noncollinear Magnetism. Noncollinear magnetism occurs when the spin magnetization density $\vec{m}(\vec{r})$ is not parallel to a global axis. Previous studies have shown the spin magnetization direction changes significantly only where the spin magnetization magnitude is small. Specifically, the spin magnetization direction stays approximately constant inside a magnetic atom but may change direction near the boundary of a magnetic atom or inside nonmagnetic atoms.[22,57−59] Since there is little variability in the magnetization direction inside individual magnetic atoms, the ASMs describe most of the essential information about the magnetic structure. As an example of noncollinear magnetism, we study the ferrous cube complex $Fe_4C_{40}H_{52}N_4O_{12}$ (commonly called $[Fe_4(sae)_4(MeOH)_4]$) synthesized and experimentally characterized by Oshio et al., which was the first example of a single-molecule magnet involving an Fe(II) cluster.[104,105] This material contains Fe and O atoms on alternating corners of a distorted cube surrounded by organic ligands. Experiments showed that this material is a single molecule magnet with an activation energy, called the magnetic anisotropy barrier, of 2.4 meV (which corresponds to 28.4 K) for reorientation of the magnetization.[104,105] This was interpreted as a ground state in which the spin moments of two Fe atoms are antiparallel along a first axis and the spin moments of the remaining two Fe atoms are antiparallel along a second axis approximately perpendicular to the first.[104] To better quantify the magnetic structure of this complex, we performed noncollinear DFT calculations in VASP using the PW91 functional with the correlation interpolation of Vosko et al.[57,61,106,107] For these simulations, the molecule was placed in the center of a $19 \times 19 \times 19$ Å^3 super cell with calculations performed at the Γ point. (See the Supporting Information for additional details.)

Finding the ground state of systems with highly noncollinear magnetism is challenging because the ASMs may point in any direction. Noncollinear calculations are commonly performed using the converged collinear magnetic structure as an initial guess.[11] This is only reliable, however, if the amount of noncollinearity is small. We developed the procedure shown in Figure 2 for finding the ground state of systems with highly noncollinear magnetism. In this procedure, spin−orbit coupling is turned off until the final geometry and four electron density components have been determined. First, the spin moments of magnetic atoms are initially set to random values, while those for nonmagnetic atoms are initially set to zero. In this example, the x, y, and z components of each Fe atom's spin moment were initialized to random values in the continuous interval between -4 and $+4$, while the spin moments for the remaining atoms were initialized to zero. The next step is to compute the energy using several such sets of random spin moments on the initial geometry. Configurations with comparatively low energy are then selected for subsequent geometry optimization. In this example, we used 12 initial sets of random spin moments and selected the six lowest energy ones for subsequent geometry optimization. Convergence of noncollinear magnetic structures can be slow because the energies for relative rotations of the spin moments can be small. As a result, the converged geometry with the lowest energy was selected for further optimization of the magnetic degrees of freedom. In this example, we continued to optimize the magnetic degrees of freedom by performing 10 ionic steps in which the atomic positions were held constant with 200 SCF cycles per ionic step, for a total of 2000 SCF cycles at the converged geometry. During this process, the molecule's total spin moment magnitude relaxed from 0.48 to 0.09. After relaxation of the magnetic degrees of freedom, the forces were rechecked, and the geometry was rerelaxed if the forces were no longer converged. In this example, the forces were still converged to better than 0.03 eV/Å, so re-relaxation of the geometry was unnecessary. This process yields the final converged geometry, four charge density components, and wave function, which are stored for use in the spin−orbit coupling calculations. Because the spin−orbit coupling energy is small, the spin−orbit coupling calculations used this saved wave function as an initial estimate and kept the geometry and four charge density components constant, except for a rotation of the spin axes. The set of possible rotations of the spin axes corresponds to the set of unit vectors from the center of a unit sphere to its surface. The spin−orbit coupling energy was computed for 60 uniformly spaced rotations defined by a grid of 60 points on the unit sphere comprising the 60 vertices of a truncated icosahedron.

After determining the system's ground state, the values $\Xi^{tot} = 5.9871$ and $\Xi^{mag} = 5.9844$ au were calculated according to eqs 55 and 53 using the finite difference approximation applied to the

4157

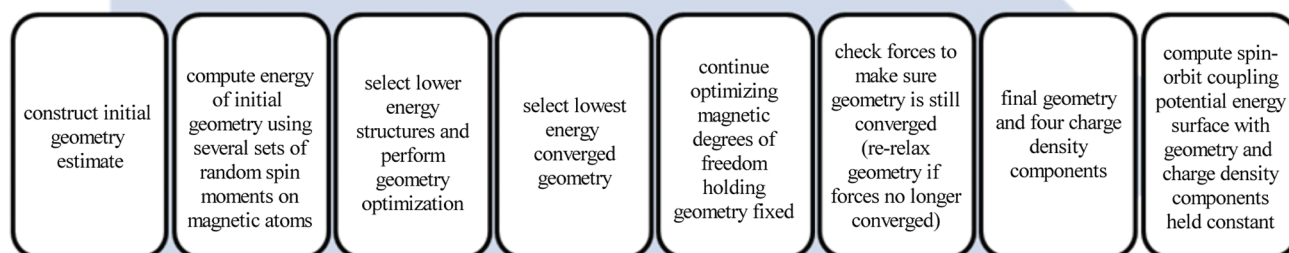dx.doi.org/10.1021/ct200539n |*J. Chem. Theory Comput.* 2011, 7, 4146–4164

Figure 2. Method for computing the ground state of systems with highly noncollinear magnetism.

same grid of $\vec{m}(\vec{r})$ values used to compute the ASMs. This gave an estimated $\Xi^{dir} = 0.0027$, which is 3 orders of magnitude smaller than Ξ^{mag}. Almost all of Ξ^{tot} is due to $m(\vec{r})$ changes, with very little due to $\hat{m}(\vec{r})$ changes, because the magnetic Fe atoms in the complex are separated by nonmagnetic atoms leading to $\hat{m}(\vec{r})$ changes only in the space between Fe atoms where $m(\vec{r}) \approx 0$. Since Ξ^{dir} is negligible, the XC energy should be accurately represented by E_{XC}^{two}. Accordingly, a GGA functional like PW91 is appropriate for modeling noncollinear magnetism in this system.

Figure 3 shows the computed ground state magnetic structure and the spin–orbit coupling potential energy surface formed by globally rotating $\vec{m}(\vec{r})$. These spin–orbit coupling interactions determine the preferred orientation of the magnetic structure relative to the molecular structure in the absence of an externally applied magnetic field. Interestingly, Figure 3 contains three minima connected by three transition states. The computed activation barrier for converting between the three minima is 2.9 meV, in good agreement with the experimental magnetic anisotropy barrier of 2.4 meV. To the best of our knowledge, experiments have not determined the number of minima on the spin–orbit coupling potential energy surface.[104] For single molecule magnets with collinear magnetism, one expects an even number of energy minima due to the symmetry between up and down spins, and model Hamiltonians for single molecule magnets usually assume an energy well with two minima.[108] If confirmed, this example of a triple-minima energy well would be a significant finding. To the best of our knowledge, spin–orbit coupling potential energy surfaces with similar features have not been previously reported.

For each atom in the complex, Bader and DDEC analysis gave essentially identical ASMs; for each atom in the molecule $|\vec{M}_A^{Bader} - \vec{M}_A^{DDEC}| \leq 0.005$. Using $\chi_{spin} = 1/2$, the ASM magnitude was 2.06 for each Fe atom and ≤ 0.10 for all other atoms. (For $\chi_{spin} = 1.0$ (3/14), these values were 2.01 (2.10) and ≤ 0.09 (0.12), respectively.) Thus, there are approximately eight magnetic electrons. ASMs converged in 1, 8, and 15 iterations for $\chi_{spin} = 1$, 1/2, and 3/14, respectively. The computed magnitude of the molecule's total spin moment was ~0.1. To the best of our
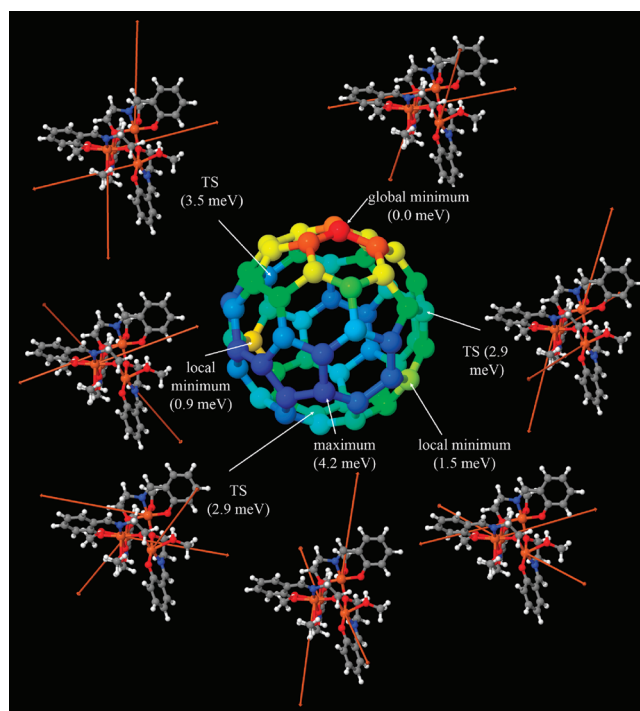

Figure 3. Spin–orbit coupling potential energy surface of the ferrous cube complex $Fe_4C_{40}H_{52}N_4O_{12}$. The center shows 60 points forming the truncated icosahedron used to sample the unit sphere of possible rotations of the spin axes, where color indicates the relative energy of each rotation. Adjacent to each labeled minimum, transition state, and maximum, the ASMs are displayed as vectors on the molecular structure, where color indicates the element (orange, Fe; red, O; blue, N; gray, C; white, H). ASMs are insignificant on all atoms except Fe. The large orange vectors show the direction and magnitude of Fe ASMs. The magnitudes and relative angles between ASMs are constant, but they rotate with respect to the molecular structure.

knowledge, experiments have not yet determined the molecule's total net spin moment at $\bar{B}_{ext} = 0$.[104] The antiparallel Fe ASMs

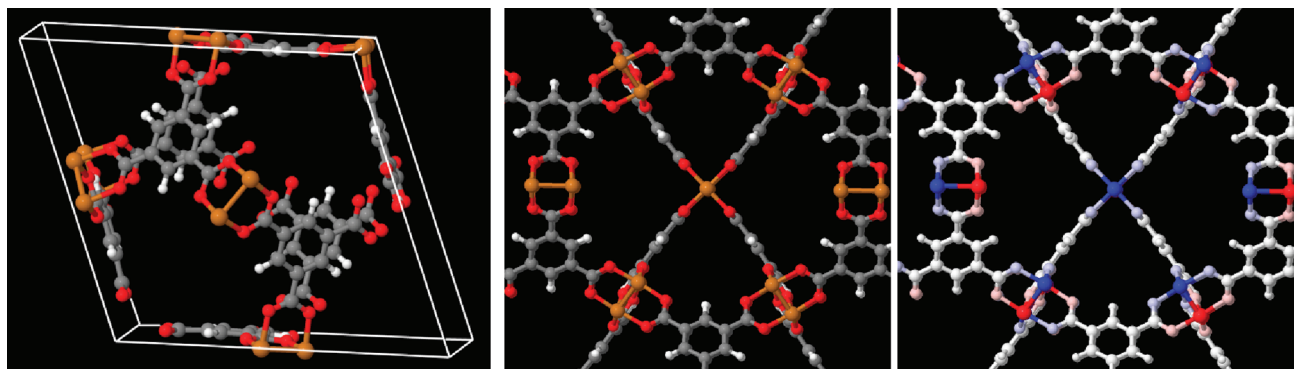**Figure 4.** The metal organic framework $Cu_3(BTC)_2$. Left: the unit cell (atoms: Cu (gold), O (red), C (gray), H(white)). Middle: looking down the pores. Right: atoms colored by ASM (−0.5 (blue) to 0.0 (white) to +0.5 (red)).

have computed angles of 178° (χ_{spin}= 1/2), indicating almost perfect antiparallelism. The first and second sets of antiparallel Fe ASMs cross at a computed 10° deviation from perpendicular. This slight deviation from perpendicular is probably due to the distorted cubic geometry.

Our calculated noncollinear magnetic structure has some important similarities and differences to previous intepretations. Oshio et al. used simple crystal field theory and the angular overlap method to interpret the experimental results. Specifically, they assumed that each Fe(II) atom was occupied by six d electrons in a high spin arrangement having four unpaired electrons.[104,109] They predicted 16 unpaired electrons ($S = 8$) for the entire molecule with a noncollinear ground state arrangement having two approximately perpendicular antiparallel pairs of Fe ASMs.[104] Our calculations show there are two approximately perpendicular antiparallel pairs of Fe ASMs in the ground state (See Figure 3) with approximately eight unpaired electrons in the molecule. Specifically, spherical harmonic projection in VASP gave 6.25 d electrons per Fe atom, and the computed ASMs showed only two d electrons per Fe atom are unpaired. Therefore, we believe the previously reported crystal field theory interpretation is incorrect, and there are eight rather than 16 unpaired electrons in the molecule. To the best of our knowledge, the only previous ab initio calculations performed for this complex are the collinear DFT calculations of Ribas-Arino et al.[110] Ribas-Arino et al. did not perform calculations to determine the ground spin state but instead restricted calculations to the $S = 8$ state suggested by Oshio et al. Using this restriction, they computed an ASM magnitude of 3.6 for each Fe atom.[110] In agreement with experiments, their results indicated that $[Fe_4(sae)_4(MeOH)_4]$ is a single molecule magnet, while the related iron cube system $[Fe_4(sap)_4(MeOH)_4]$ is not.[104,110] They computed a magnetic anisotropy barrier of 0.5 meV for $[Fe_4(sae)_4(MeOH)_4]$, which is not nearly as close to the experimental value of 2.4 meV as our computed value of 2.9 meV. Our ab initio calculations are the first to consider noncollinear magnetism for this complex.

Experiments performed from near absolute zero temperature to above room temperature showed that $[Fe_4(sae)_4(MeOH)_4]$ has a positive magnetic susceptibility, meaning that the net magnetic moment increases in the direction of an applied magnetic field.[104,105] Within the framework of the $S = 8$ spin model described above, Oshio et al. and Ribas-Arino et al. interpreted the positive magnetic susceptibility as an increasing occupation of the $S_Z = +8$ state at the expense of the $S_Z = -8$ state as the external magnetic field is increased.[104,105,110]

Our noncollinear DFT computations provide a different explanation for the positive magnetic susceptibility. Specifically, our calculations showed that the net spin moment magnitude M could be changed from 0.09 to 0.48 with only a 0.17 meV increase in total energy, which is an order of magnitude lower than the magnetization reorientation energy barrier. The magnitude of each Fe ASM remained constant at 2.06 during this increase in M, while the angles between them changed slightly. This means that the Fe ASMs can undergo small relative rotations with little change in the total energy. These calculations were performed with no external magnetic field applied. When an external magnetic field $\vec{B}_{ext}$ is applied, an energy of $g_e \mu_B \vec{M} \cdot \vec{B}_{ext}/2$ must be included in the system's Hamiltonian; therefore, to minimize the system's energy in the presence of nonzero $\vec{B}_{ext}$, the Fe spin moments will rotate so as to increase $\vec{M}/2$ in the direction of the applied magnetic field. Our results strongly suggest that the individual Fe ASMs in the noncollinear arrangement can easily rotate toward the direction of an externally applied magnetic field, leading to a change in the angles between Fe ASMs. In summary, our calculations for $\vec{B}_{ext} = 0$ give a ground state having (a) eight unpaired electrons with an ASM of ~2.06 on each Fe atom, (b) small spin moments on all atoms except Fe, (c) noncollinear magnetism in which four Fe spin moments are aligned in two pairs with antiparallel alignment within a pair and a deviation of ~10° from perpendicular between pairs, (d) a magnetization reorientation barrier of ~2.9 meV with a triple-minima energy, and (e) $M \approx$ 0.1. For $\vec{B}_{ext} \neq 0$, a positive magnetic susceptibility is predicted due to canting of the noncollinear Fe spin moments. The computational techniques described here will also be useful to better understand the properties of other noncollinear magnetic systems.

4.4. The Antiferromagnetic Metal Organic Framework $Cu_3(BTC)_2$. In the above sections, ASMs have been computed for nonporous solids and molecular systems. We now consider a porous solid. The metal−organic framework Cu_3(benzenetricarboxylate)$_2$, abbreviated $Cu_3(BTC)_2$, has open metal sites that can bind adsorbates and is widely studied for gas adsorption and catalytic applications.[65,111−116] This material has high adsorption capacities for acetylene and nitric oxide,[115,116] is a Lewis acid catalyst for several molecular rearrangement reactions,[111] and activates molecules for liquid phase cyanosilylation.[114] Figure 4 shows the unit cell of $Cu_3(BTC)_2$ containing 156 atoms. The copper atoms are arranged in pairs with a Cu−Cu bond length of ~2.5 Å. The distance between adjacent Cu pairs is ~10 Å. Oxygen atoms connect the Cu pairs to aromatic linking groups. Temperature-dependent magnetic susceptibility and electron

Table 5. Magnitude of ASMs for $Cu_3(BTC)_2$

		NAC		ASM				
	oxidation state	Bader	DDEC	Bader	$\chi_{spin} = 1.0$	$\chi_{spin} = 3/14$	$\chi_{spin} = 1/2$	LSF
Cu	2	1.04	0.89	0.49	0.49	0.48	0.49	0.47
O	−2	−1.09	−0.56	0.09	0.09	0.09	0.09	0.10
other atoms				<0.01	<0.01	<0.01	<0.01	<0.01
iterations[a]					1	12	6	39

[a] Iterations required to converge ASMs to within 5×10^{-5}.

Table 6. Population Analysis for Spin States of Ozone

method	total S_z	Δ_S	relative energy (eV)	O−O−O angle (deg)	O−O dist. (Å)	net charge	O−O−O NAC[a]	O−O−O ASM[a]	O−O−O NAC[b]	O−O−O ASM[b]
				singlet state						
exp.	0		0	116.8[c]	1.27[c]					
B3LYP	0	0	0	118.5	1.26	0	0.39	0.00	−0.20	0.00
PW91	0	0	0	118.4	1.28	0	0.37	0.00	−0.18	0.00
CCSD	0	0	0	117.8	1.24	0	0.37	0.00	−0.18	0.00
SAC−CI	0	0	0	117.8	1.24	0	0.40	0.00	−0.20	0.00
				triplet states						
exp.	1		1.18[d]	98.9[e]	1.35[e]					
B3LYP	1	0.01	0.82	99.2	1.32	0	0.20	0.38	−0.10	0.81
PW91	1	0.01	0.96	99.3	1.35	0	0.20	0.38	−0.10	0.81
CCSD	1	<0.08[g]	1.06	97.5	1.32	0	0.23	0.42	−0.12	0.79
SAC−CI	0	0	1.30	97.4	1.32	0	0.20	0.00	−0.10	0.00
				+1 cation doublet state						
exp.	1/2		12.52[f]	131.5[f]	1.25[f]					
B3LYP	1/2	0.01	12.74	134.6	1.21	1	0.53	0.22	0.24	0.39
PW91	1/2	0.00	12.35	134.3	1.23	1	0.48	0.20	0.26	0.40
CCSD	1/2	<0.03[g]	12.71	133.4	1.18	1	0.49	0.24	0.26	0.38

[a] DDEC NAC and ASM ($\chi_{spin} = 1/2$) of the center oxygen atom. [b] DDEC NAC and ASM ($\chi_{spin} = 1/2$) of each outer oxygen atom. [c] Ref 121. [d] Ref 122. [e] Ref 123. [f] Ref 124. [g] Δ_S values for the HF reference configuration were used as an upper bound for the CCSD Δ_S values.

spin resonance experiments show that the Cu atoms have strong antiferromagnetic coupling within a pair and weak ferromagnetic coupling between pairs.[117−119] Electron paramagnetic resonance (EPR) showed that the arrangement of ASMs was not static; there was dynamic spin exchange between the Cu atoms, as evidenced by the broad EPR peaks.[119] Thus, a particular Cu atom is not locked into a spin-up or -down orientation but rather switches between the two on some short time scale. Watanabe and Sholl showed that the PW91 functional correctly predicts the antiferromagnetic ground state of this material.[65] Using this functional, the ASMs for Cu and O have magnitudes of 0.49 and 0.09, respectively, as shown in Table 5. The ASMs were not sensitive to the choice of population analysis method, but the NACs were. The sign of each ASM is shown on the right side of Figure 4.

4.5. Ozone. As a final example, we computed ASMs for singlet, triplet, and cation doublet states of ozone using DFT and coupled cluster expansions with 6-311+G* basis sets. For the coupled cluster expansions, CCSD was used to compute the singlet, $S_Z = +1/2$ doublet, and $S_Z = +1$ triplet states, while the symmetry adapted cluster configuration interaction (SAC−CI) method of Nakatsuji et al.[45,46,120] was used to compute the singlet and $S_Z = 0$

triplet states. SAC−CI is a coupled cluster expansion that includes symmetry operators for computing the $S_Z = 0$ ground and excited states.[45,46,120] Except for a flip of the spin direction, the $S_Z = -1/2$ doublet and $S_Z = -1$ triplet states (not shown) are identical to the $S_Z = +1/2$ doublet and $S_Z = +1$ triplet states, respectively. As shown in Table 6, for each spin state, the optimized geometries and relative energies are in good agreement with the experimental value. We find that the computed ASMs are similar for the CCSD and DFT methods. The small DFT Δ_S values indicate that the spin densities can be accurately reproduced by DFT. Our results suggest that DFT and CCSD give similar ASMs when Δ_S is small.

5. CONCLUSIONS

A functional for optimizing atomic spin moments (ASMs) using the DDEC atomic density distributions was presented that has a unique minimum. These ASMs are especially suitable for constructing interaction potentials for atomistic simulations, because they accurately reproduce the spin-derived magnetic field component, $\vec{B}^{spin}(\vec{r})$, outside a material's electron distribution as well as the chemical states of atoms in a material. The parameter

4160

dx.doi.org/10.1021/ct200539n |J. Chem. Theory Comput. 2011, 7, 4146−4164

χ_{spin}, which determines the relative weights of proportional and spherically averaged atomic spin density in this functional, had a small influence on the ASM values. We recommend the value $\chi_{\text{spin}} = 1/2$, which gives converged ASMs in fewer than 10 iterations and is accurate for reproducing both $\vec{B}^{\text{spin}}(\vec{r})$ and the chemical states of atoms. This functional performed better than a functional that minimizes the least squared difference between the local and spherically averaged atomic spin magnetization densities.

Results showed that the computational method (i.e., DFT, DFT+U, coupled-cluster, etc.) has a larger influence on the computed ASMs than the population analysis method (i.e., Bader, NPA, DDEC). The Bader, DDEC, and (where applicable) NPA methods gave similar ASMs, but different net atomic charges. Bader and DDEC ASMs have the advantage of being applicable to periodic and nonperiodic materials and to collinear and noncollinear magnetism. The computed ASMs were in good agreement with available experimental data for a variety of periodic and nonperiodic materials. A range of materials exhibiting collinear magnetism were studied, including diatomic iodides, an antiferromagnetic metal organic framework, $Cu_3(BTC)_2$, several ozone spin states, mono- and binuclear transition metal complexes, and ferri- and ferro-magnetic solids (Fe_3O_4 and Fe_3Si). The highly correlated material magnetite was studied using DFT+U and HSE06 methods. In agreement with prior literature, we found that the U_{eff} parameter has a large effect on charge and spin ordering in mixed oxidation state materials like magnetite. Both DFT+U and HSE06 separate octahedral Fe sites into nominally Fe^{II} and Fe^{III} atoms with different net charges and ASMs, while PBE calculations give only one type of octahedral Fe.

Noncollinear magnetic calculations are usually started using the converged collinear magnetic structure as an initial guess. This procedure is only reliable, however, when the amount of noncollinearity is small. We developed a procedure for finding the ground state of systems with highly noncollinear magnetism. The single-molecule magnet $Fe_4C_{40}H_{52}N_4O_{12}$ was studied by this method. The computed ground state magnetic structure was highly noncollinear and provided an improved explanation of the experimental results. Also, we briefly discussed the theory of XC functionals for studying noncollinear magnetism and introduced two descriptors, Ξ^{dir} and Ξ^{mag}, that are helpful for choosing an appropriate XC functional when studying noncollinear magnetism.

■ APPENDIX

1. Proof H Has a Unique Minimum. The core of the method we have introduced is the minimization of the functional H defined in eq 29. We now show that H has only one minimum. To prove uniqueness, it is sufficient to show that H is everywhere convex, which is necessarily true if its second-order variational derivative

$$\delta^2 H = \sum_A \sum_B \oint \oint \delta \vec{m}_A(\vec{r}_A) \cdot \frac{\partial^2 H}{\partial \vec{m}_A(\vec{r}_A) \partial \vec{m}_B(\vec{r}'_B)} \cdot \delta \vec{m}_B(\vec{r}'_B) \, d^3 \vec{r}_A \, d^3 \vec{r}'_B \quad (67)$$

is greater than or equal to zero for arbitrary $\{\delta \vec{m}_A(\vec{r}_A)\}$. Since the only non-zero second order derivatives of H with respect to the independent variables $\{\vec{m}_A(\vec{r}_A)\}$ are

$$\frac{\partial^2 H}{\partial \vec{m}_A(\vec{r}_A) \partial \vec{m}_A(\vec{r}'_A)} = \frac{1}{2} \oint_\omega \frac{\partial}{\partial \vec{m}_A(\vec{r}'_A)} \ln\left(\frac{\rho_A(\vec{r}_A, \hat{h})}{w_A^{\text{spin}}(\vec{r}_A, \hat{h})}\right) \hat{h} \, d^2\omega$$
$$+ \nu_A(\vec{r}_A) \frac{\partial \hat{m}_A(\vec{r}_A)}{\partial \vec{m}_A(\vec{r}'_A)} \quad (68)$$

it follows from eq 67 that H is convex if

$$\oint \oint \vec{\varphi}(\vec{r}_A) \cdot \frac{\partial^2 H}{\partial \vec{m}_A(\vec{r}_A) \partial \vec{m}_A}(\vec{r}'_A) \cdot \vec{\varphi}(\vec{r}'_A) \, d^3 \vec{r}_A \, d^3 \vec{r}'_A \geq 0 \quad (69)$$

for every real-valued differentiable function $\vec{\varphi}(\vec{r}_A)$. Expanding,

$$\frac{\partial \hat{m}_A(\vec{r}_A)}{\partial \vec{m}_A(\vec{r}'_A)}$$
$$= \left(\frac{\hat{x}\hat{x} + \hat{y}\hat{y} + \hat{z}\hat{z} - \hat{m}_A(\vec{r}_A)\hat{m}_A(\vec{r}_A)}{m_A(\vec{r}_A)}\right)\delta^{\text{dirac}}(\vec{r}'_A - \vec{r}_A) \quad (70)$$

gives

$$\oint \oint \vec{\varphi}(\vec{r}_A) \cdot \nu_A(\vec{r}_A) \frac{\partial \hat{m}_A(\vec{r}_A)}{\partial \vec{m}_A(\vec{r}'_A)} \cdot \vec{\varphi}(\vec{r}'_A) \, d^3 \vec{r}_A \, d^3 \vec{r}'$$
$$= \oint \nu_A(\vec{r}_A) \frac{|\vec{\varphi}(\vec{r}_A)|^2 - |\vec{\varphi}(\vec{r}_A) \cdot \hat{m}_A(\vec{r}_A)|^2}{m_A(\vec{r}_A)} \, d^3 \vec{r}_A \geq 0 \quad (71)$$

The inequality in eq 71 follows from the fact that $\nu_A(\vec{r}_A) \geq 0$ and the absolute value of the scalar projection of a vector onto any unit direction is less than or equal to the magnitude of that vector. Expanding

$$\frac{\partial}{\partial \vec{m}_A(\vec{r}'_A)} \ln\left(\frac{\rho_A(\vec{r}_A, \hat{h})}{w_A^{\text{spin}}(\vec{r}_A, \hat{h})}\right)$$
$$= \hat{h}\left(\frac{\delta^{\text{dirac}}(\vec{r}'_A - \vec{r}_A)}{2\rho_A(\vec{r}_A, \hat{h})} - \frac{(1 - \chi_{\text{spin}})\delta^{\text{dirac}}(r'_A - r_A)}{8\pi(r_A)^2 \rho_A^{\text{avg}}(r_A, \hat{h})}\right) \quad (72)$$

gives

$$\oint \oint \vec{\varphi}(\vec{r}_A) \cdot \hat{h} \frac{\partial}{\partial \vec{m}_A}(\vec{r}'_A) \ln\left(\frac{\rho_A(\vec{r}_A, \hat{h})}{w_A^{\text{spin}}(\vec{r}_A, \hat{h})}\right) \hat{h} \vec{\varphi}(\vec{r}'_A) \, d^3 \vec{r}_A \, d^3 \vec{r}'_A$$
$$= \oint \frac{|\vec{\varphi}(\vec{r}_A) \cdot \hat{h}|^2}{2\rho_A(\vec{r}_A, \hat{h})} \, d^3 \vec{r}_A - (1 - \chi_{\text{spin}}) \oint \frac{|\vec{\varphi}(\vec{r}_A) \cdot \hat{h}||\vec{\varphi}^{\text{avg}}(r_A) \cdot \hat{h}|}{2\rho_A^{\text{avg}}(r_A, \hat{h})} \, d^3 \vec{r}_A$$
$$= \oint \left(\frac{|\vec{\varphi}(\vec{r}_A) \cdot \hat{h}|^2}{2\rho_A(\vec{r}_A, \hat{h})} - (1 - \chi_{\text{spin}}) \frac{|\vec{\varphi}^{\text{avg}}(r_A) \cdot \hat{h}|^2}{2\rho_A^{\text{avg}}(r_A, \hat{h})}\right) d^3 \vec{r}_A \geq 0 \quad (73)$$

Bultinck et al. showed that

$$\oint \left(\frac{f(\vec{r}_A)^2}{g_A(\vec{r}_A)} - \frac{f^{\text{avg}}(r_A)^2}{g_A^{\text{avg}}(r_A)}\right) d^3 \vec{r}_A \geq 0 \quad (74)$$

for any differentiable real-valued functions $g_A(\vec{r}_A) \geq 0$ and $f(\vec{r}_A)$.[125] Thus, by setting $f(\vec{r}_A) = \vec{\varphi}(\vec{r}_A) \cdot \hat{h}$ and $g_A(\vec{r}_A) = 2\rho_A(\vec{r}_A, \hat{h})$, it follows that the integral in eq 73 is positive definite. Combining eqs 67, 68, 71, and 73 gives $\delta^2 H \geq 0$, which proves that H has a unique minimum.

2. Algorithm for Computing the Inverse of $\xi(\tau)$. The iterative scheme defined in section 3.1 requires calculating the

inverse of $\gamma = \xi(\tau)$, denoted $\xi^{\text{inv}}(\gamma)$. This quantity was computed by Newton's method starting from an initial estimate of

$$\xi^{\text{inv}}(\gamma)\big|_0 = \frac{\gamma + a_1\gamma^2}{a_2 + a_3\gamma + a_4\gamma^2}, 0 \le \gamma \le 2\pi \tag{75}$$

The constants $a_1 = -0.036835$, $a_2 = 4.178319$, $a_3 = -0.136129$, and $a_4 = 0.038148$ were determined by fitting the points $\gamma = 0$, $\pi/2$, π, $3\pi/2$, and 2π. Newton's method gives the refined value at iteration $(j+1)$ in terms of the error and derivative at iteration j; specifically,

$$\xi^{\text{inv}}(\gamma)\big|_{j+1} = \xi^{\text{inv}}(\gamma)\big|_j + \frac{\gamma - \xi(\xi^{\text{inv}}(\gamma)\big|_j)}{\xi'(\xi^{\text{inv}}(\gamma)\big|_j)} \tag{76}$$

where the derivative is

$$\xi'(\tau) = \frac{2\pi}{\tau^3}\left(\ln\left(\frac{1+\tau}{1-\tau}\right) - 2\tau\right), \xi'(0) = 4\pi/3 \tag{77}$$

$\xi(\tau)$ was expanded near $\tau = 0$ and 1 to avoid singularities in eqs 35 and 77: (a) $\xi(\tau) \approx 4\pi\tau/3$ and $\xi'(\tau) \approx 4\pi/3$ for $\tau \le 0.001$ and (b) $\xi(\tau) \approx 2\pi + 49.956(\tau - 1) + 8370.6(\tau - 1)^2$ and $\xi'(\tau) \approx 50.0$ for $\tau \ge 0.999$. Two Newton iterations were sufficient to achieve at least four significant digits of accuracy over the entire range of τ values.

3. Derivation of the Value $c = \pi$ in eq 59. Since eq 64 imposes constraint 11 for any positive value of c, the value of c has no effect on the converged solution. It does, however, affect the number of iterations required to reach convergence. To minimize the number of iterations required to reach convergence, the value $c = \pi$ derived here should be used. Using the subscripts j and $(j-1)$ to indicate assignments for the current iteration (i.e., j) based on quantities for the last iteration (i.e., $j - 1$), eq 59 is

$$\vec{L}_A(\vec{r}_A)\big|_j = \vec{Y}(\vec{r})\big|_{j-1} - \vec{\Omega}(\vec{r})\big|_{j-1}$$
$$+ c\frac{(\vec{m}(\vec{r}) - \vec{m}^{\text{trial}}(\vec{r}))}{\rho(\vec{r})}\bigg|_{j-1} + \vec{\eta}_A(\vec{r}_A)\big|_{j-1} \tag{78}$$

Multiplying both sides by $\rho_A(\vec{r}_A)/\rho(\vec{r})$ and summing over A gives

$$\vec{Y}(\vec{r})\big|_j - \vec{Y}(\vec{r})\big|_{j-1} = c\frac{(\vec{m}(\vec{r}) - \vec{m}^{\text{trial}}(\vec{r})\big|_{j-1})}{\rho(\vec{r})} \tag{79}$$

To satisfy constraint 11 in iteration j, we should have

$$\vec{m}^{\text{trial}}(\vec{r})\big|_j \approx \vec{m}(\vec{r}) \tag{80}$$

Inserting eq 80 into the right-hand side of eq 79 gives

$$\vec{Y}(\vec{r})\big|_j - \vec{Y}(\vec{r})\big|_{j-1} \approx \frac{c}{\rho(\vec{r})}(\vec{m}^{\text{trial}}(\vec{r})\big|_j - \vec{m}^{\text{trial}}(\vec{r})\big|_{j-1}) \tag{81}$$

Defining

$$\Delta m_A(\vec{r}_A) = m_A(\vec{r}_A)\big|_j - m_A(\vec{r}_A)\big|_{j-1} \tag{82}$$

Equation 81 can be rewritten as

$$\frac{\partial \vec{Y}(\vec{r})}{\partial m_A(\vec{r}_A)}\Delta m_A(\vec{r}_A) \approx \frac{c}{\rho(\vec{r})}\Delta m_A(\vec{r}_A) \tag{83}$$

Using eqs 61 and 37, the derivative can be expanded as

$$\frac{\partial \vec{Y}(\vec{r})}{\partial m_A(\vec{r}_A)} = \frac{\rho_A(\vec{r}_A)}{\rho(\vec{r})}\frac{\partial L_A(\vec{r}_A)}{\partial m_A(\vec{r}_A)} = \frac{1}{2\rho(\vec{r})}\frac{\partial \xi(\tau)}{\partial \tau} \tag{84}$$

Comparing eqs 83 and 84, one-half the average value of the derivative of $\xi(\tau)$ over the range of possible τ values (i.e. $\tau = 0$ to 1) is a good choice for c:

$$c \approx \frac{1}{2}\frac{\partial \xi(\tau)}{\partial \tau} \approx \frac{\xi(1) - \xi(0)}{2} = \frac{2\pi - 0}{2} = \pi \tag{85}$$

In practice, we found that using $c = \pi$ converges $\vec{m}^{\text{trial}}(\vec{r})$ to $\vec{m}(\vec{r})$ in just a couple of iterations.

■ ASSOCIATED CONTENT

ⓢ Supporting Information. Coordinates of optimized geometries, more extensive results tables, example input files, set of grid points used to compute the MAE and RMAE of $\vec{B}_{\text{spin}}(\vec{r})$, and computational algorithm and uniqueness proof for the LSF functional that computes ASMs by minimizing $|\vec{m}_A(\vec{r}_A) - \vec{m}_A^{\text{avg}}(\vec{r}_A)|^2/\rho_A^{\text{avg}}(\vec{r}_A)$ subject to constraints 11 and 26. This material is available free of charge via the Internet at http://pubs.acs.org.

■ AUTHOR INFORMATION

Corresponding Author
*E-mail: thomasamanz@gmail.com, david.sholl@chbe.gatech.edu.

■ ACKNOWLEDGMENT

■ REFERENCES

(1) Back, C. H.; Wursch, C.; Vaterlaus, A.; Ramsperger, U.; Maier, U.; Pescia, D. *Nature* **1995**, *378*, 597–600.
(2) Rosenbaum, T. F.; Silevitch, D. M.; Bitko, D.; Brooke, J.; Ghosh, S.; Aeppli, G. *Nature* **2007**, *448*, 567–570.
(3) Zhang, W. M.; Saslow, W. M.; Gabay, M.; Benakli, M. *Phys. Rev. B* **1993**, *48*, 10204–10216.
(4) Bader, R. F. W. *J. Phys. Chem. A* **2007**, *111*, 7966–7972.
(5) Bader, R. F. W.; Macdougall, P. J.; Lau, C. D. H. *J. Am. Chem. Soc.* **1984**, *106*, 1594–1605.
(6) Hirshfeld, F. L. *Theor. Chim. Acta* **1977**, *44*, 129–138.
(7) Reed, A. E.; Weinstock, R. B.; Weinhold, F. *J. Chem. Phys.* **1985**, *83*, 735–746.
(8) Philips, J. J.; Hudspeth, M. A.; Browne, P. M.; Peralta, J. E. *Chem. Phys. Lett.* **2010**, *495*, 146–150.
(9) Macdougall, P. J.; Bader, R. F. W. *Can. J. Chem.* **1986**, *64*, 1496–1508.
(10) Mulliken, R. S. *J. Chem. Phys.* **1955**, *23*, 1833–1840.

(11) Kresse, G.; Marsman, M.; Furthmüller, J. *VASP the Guide*; Universitat Wien: Vienna, Austria, 2011. http://cms.mpi.univie.ac.at/vasp/vasp/vasp.html (accessed July 26, 2011).

(12) Bultinck, P.; Van Alsenoy, C.; Ayers, P. W.; Carbo-Dorca, R. *J. Chem. Phys.* **2007**, *126*, 144111.

(13) Davidson, E. R.; Chakravorty, S. *Theor. Chim. Acta* **1992**, *83*, 319–330.

(14) Manz, T. A.; Sholl, D. S. *J. Chem. Theory Comput.* **2010**, *6*, 2455–2468.

(15) Montgomery, J. A.; Frisch, M. J.; Ochterski, J. W.; Petersson, G. A. *J. Chem. Phys.* **2000**, *112*, 6532–6542.

(16) Watanabe, T.; Manz, T. A.; Sholl, D. S. *J. Phys. Chem. C* **2011**, *115*, 4824–4836.

(17) Kim, H. W.; Jung, J.; Han, M. N.; Lim, S.; Tamada, K.; Hara, M.; Kawa, M.; Kim, Y.; Kuk, Y. *J. Am. Chem. Soc.* **2011**, *133*, 9236–9238.

(18) Dirac, P. A. M. *Proc. R. Soc., London A* **1928**, *118*, 351–361.

(19) Dirac, P. A. M. *Proc. R. Soc., London A* **1928**, *117*, 610–624.

(20) Foldy, L. L.; Wouthuysen, S. A. *Phys. Rev.* **1950**, *78*, 345–345.

(21) Szabo, A.; Ostlund, N. S. *Modern Quantum Chemistry*; Dover: Mineola, NY, 1996; pp 97–107.

(22) Peralta, J. E.; Scuseria, G. E.; Frisch, M. J. *Phys. Rev. B* **2007**, *75*, 125119.

(23) van Lenthe, E.; Snijders, J. G.; Baerends, E. J. *J. Chem. Phys.* **1996**, *105*, 6505–6516.

(24) Closs, G. L.; Forbes, M. D. E.; Piotrowiak, P. *J. Am. Chem. Soc.* **1992**, *114*, 3285–3294.

(25) Gidopoulos, N. I. *Phys. Rev. B* **2007**, *75*, 134408.

(26) Ivanovic, I. D. *J. Phys. A* **1993**, *26*, L579–L582.

(27) Wittbrodt, J. M.; Schlegel, H. B. *J. Chem. Phys.* **1996**, *105*, 6574–6577.

(28) Cohen, A. J.; Tozer, D. J.; Handy, N. C. *J. Chem. Phys.* **2007**, *126*, 214104.

(29) Nakatsuji, S.; Machida, Y.; Onoda, S.; Tayama, T.; Sakakibara, T. *Nature* **2010**, *463*, 210–213.

(30) Evans, P. G.; Isaacs, E. D.; Aeppli, G.; Cai, Z.; Lai, B. *Science* **2002**, *295*, 1042–1045.

(31) Gingras, M. J. P.; Bramwell, S. T. *Science* **2001**, *294*, 1495–1501.

(32) Lee, S. H.; Broholm, C.; Ratcliff, W.; Gasparovic, G.; Huang, Q.; Kim, T. H.; Cheong, S. W. *Nature* **2002**, *418*, 856–858.

(33) Shpyrko, O. G.; Isaacs, E. D.; Logan, J. M.; Feng, Y. J.; Aeppli, G.; Jaramillo, R.; Kim, H. C.; Rosenbaum, T. F.; Zschack, P.; Sprung, M.; Narayanan, S.; Sandy, A. R. *Nature* **2007**, *447*, 68–71.

(34) Perdew, J. P.; Ruzsinszky, A.; Constantin, L. A.; Sun, J. W.; Csonka, G. I. *J. Chem. Theory Comput.* **2009**, *5*, 902–908.

(35) Barth, U. V.; Hedin, L. *J. Phys. C* **1972**, *5*, 1629–1642.

(36) Pople, J. A.; Gill, P. M. W.; Handy, N. C. *Int. J. Quantum Chem.* **1995**, *56*, 303–305.

(37) Grafenstein, J.; Kraka, E.; Cremer, D. *Chem. Phys. Lett.* **1998**, *288*, 593–602.

(38) Grafenstein, J.; Kraka, E.; Filatov, M.; Cremer, D. *Int. J. Mol. Sci.* **2002**, *3*, 360–394.

(39) Perdew, J. P.; Savin, A.; Burke, K. *Phys. Rev. A* **1995**, *51*, 4531–4541.

(40) Caballol, R.; Castell, O.; Illas, F.; Moreira, P. R.; Malrieu, J. P. *J. Phys. Chem. A* **1997**, *101*, 7860–7866.

(41) Grimme, S.; Waletzke, M. *J. Chem. Phys.* **1999**, *111*, 5645–5655.

(42) Ullrich, C. A.; Kohn, W. *Phys. Rev. Lett.* **2001**, *87*, 093001.

(43) van Leeuwen, R. *Adv. Quantum Chem.* **2003**, *43*, 25–94.

(44) Dreizler, R. M.; Gross, E. K. U. *Density Functional Theory*; Springer: Berlin, 1990; pp 54–61.

(45) Nakatsuji, H. *Chem. Phys. Lett.* **1979**, *67*, 329–333.

(46) Nakatsuji, H.; Hirao, K. *J. Chem. Phys.* **1978**, *68*, 2053–2065.

(47) Ehara, M.; Kuramoto, K.; Nakatsuji, H. *Chem. Phys.* **2009**, *356*, 195–198.

(48) Geertsen, J.; Rittby, M.; Bartlett, R. J. *Chem. Phys. Lett.* **1989**, *164*, 57–62.

(49) Evangelista, F. A. *J. Chem. Phys.* **2011**, *134*, 224102.

(50) Ruiz, E.; Cirera, J.; Alvarez, S. *Coord. Chem. Rev.* **2005**, *249*, 2649–2660.

(51) Lillestolen, T. C.; Wheatley, R. J. *Chem. Commun.* **2008**, 5909–5911.

(52) Good, R. H.; Nelson, T. J. *Classical Theory of Electric and Magnetic Fields*; Academic Press: New York, 1971, pp 219–220, 465–466.

(53) Panofsky, W. K. H.; Phillips, M. *Classical Electricity and Magnetism*; Addison-Wesley: Reading, MA, 1962; pp 130–133.

(54) Campana, C.; Mussard, B.; Woo, T. K. *J. Chem. Theory Comput.* **2009**, *5*, 2866–2878.

(55) Capelle, K.; Vignale, G.; Gyorffy, B. L. *Phys. Rev. Lett.* **2001**, *87*, 206403.

(56) Sharma, S.; Dewhurst, J. K.; Ambrosch-Draxl, C.; Kurth, S.; Helbig, N.; Pittalis, S.; Shallcross, S.; Nordstrom, L.; Gross, E. K. U. *Phys. Rev. Lett.* **2007**, *98*, 196405.

(57) Hobbs, D.; Kresse, G.; Hafner, J. *Phys. Rev. B* **2000**, *62*, 11556–11570.

(58) Oda, T.; Pasquarello, A.; Car, R. *Phys. Rev. Lett.* **1998**, *80*, 3622–3625.

(59) Knopfle, K.; Sandratskii, L. M.; Kubler, J. *Phys. Rev. B* **2000**, *62*, 5564–5569.

(60) Tsunoda, Y.; Nishioka, Y.; Nicklow, R. M. *J. Magn. Magn. Mater.* **1993**, *128*, 133–137.

(61) Hafner, J. *J. Comput. Chem.* **2008**, *29*, 2044–2078.

(62) Kresse, G.; Furthmuller, J. *Phys. Rev. B* **1996**, *54*, 11169–11186.

(63) Kresse, G.; Joubert, D. *Phys. Rev. B* **1999**, *59*, 1758–1775.

(64) Frisch, M. J.; Trucks, G. W.; Schlegel, H. B.; Scuseria, G. E.; Robb, M. A.; Cheeseman, J. R.; Scalmani, G.; Barone, V.; Mennucci, B.; Petersson, G. A.; Nakasuji, H.; Caricato, M.; Li, X.; Hratchian, H. P.; Izmaylov, A. F.; Bloino, J.; Zheng, G.; Sonnenberg, J. L.; Hada, M.; Ehara, M.; Toyota, K.; Fukuda, R.; Hasegawa, J.; Ishida, M.; Nakamjima, T.; Honda, Y.; Kitao, O.; Nakai, H.; Vreven, T.; Montgomery, J. A., Jr.; Peralta, J. E.; Ogliaro, F.; Bearpark, M.; Heyd, J. J.; Brothers, E.; Kudin, K. N.; Staroverov, V. N.; Kobayashi, R.; Normand, J.; Raghavachari, K.; Rendell, A.; Burant, J. C.; Iyengar, S. S.; Tomasi, J.; Cossi, M.; Rega, N.; Millam, N. J.; Klene, M.; Knox, J. E.; Cross, J. B.; Bakken, V.; Adamo, C.; Jaramillo, J.; Gomperts, R.; Stratmann, R. E.; Yazyev, O.; Austin, A. J.; Cammi, R.; Pomelli, C.; Ochterski, J. W.; Martin, R. L.; Morokuma, K.; Zakrzewski, V. G.; Voth, G. A.; Salvador, P.; Dannenberg, J. J.; Dapprich, S.; Daniels, A. D.; Farkas, O.; Foresman, J. B.; Ortiz, J. V.; Ciolowski, J.; Fox, D. J. *Gaussian 09*, Revision A.02; Gaussian, Inc.: Wallingford, CT, 2009.

(65) Watanabe, T.; Sholl, D. S. *J. Chem. Phys.* **2010**, *133*, 094509.

(66) Zuxiang, Y. *Rock Miner. Anal.* **1984**, *3*, 231–238.

(67) Louie, S. G.; Froyen, S.; Cohen, M. L. *Phys. Rev. B* **1982**, *26*, 1738–1742.

(68) Krauss, M.; Stevens, W. J. *Annu. Rev. Phys. Chem.* **1984**, *35*, 357–385.

(69) Henkelman, G.; Arnaldsson, A.; Jonsson, H. *Comput. Mater. Sci.* **2006**, *36*, 354–360.

(70) Sanville, E.; Kenny, S. D.; Smith, R.; Henkelman, G. *J. Comput. Chem.* **2007**, *28*, 899–908.

(71) Tang, W.; Sanville, E.; Henkelman, G. *J. Phys. Cond. Matter* **2009**, *21*, 084204.

(72) Cao, W. L.; Gatti, C.; Macdougall, P. J.; Bader, R. F. W. *Chem. Phys. Lett.* **1987**, *141*, 380–385.

(73) Glendening, E. D.; Reed, A. E.; Carpenter, J. E.; Weinhold, F. *NBO 3.0 Program Manual*; University of Wisconsin: Madison, WI, 1990; pp A.1–B.56.

(74) Perdew, J. P.; Burke, K.; Ernzerhof, M. *Phys. Rev. Lett.* **1996**, *77*, 3865–3868.

(75) Singh, U. C.; Kollman, P. A. *J. Comput. Chem.* **1984**, *5*, 129–145.

(76) Aebersold, M. A.; Gillon, B.; Plantevin, O.; Pardi, L.; Kahn, O.; Bergerat, P.; von Seggern, I.; Tuczek, F.; Ohrstrom, L.; Grand, A.; Lelievre-Berna, E. *J. Am. Chem. Soc.* **1998**, *120*, 5238–5245.

(77) Figgis, B. N.; Forsyth, J. B.; Reynolds, P. A. *Inorg. Chem.* **1987**, *26*, 101–105.

(78) Hines, W. A.; Menotti, A. H.; Budnick, J. I.; Burch, T. J.; Litrenta, T.; Niculescu, V.; Raj, K. *Phys. Rev. B* **1976**, *13*, 4060–4068.

(79) Wenzel, M. J.; Steinle-Neumann, G. *Phys. Rev. B* **2007**, *75*, 214430.

(80) Verwey, E. J. W. *Nature* **1939**, *144*, 327–328.

(81) Shchennikov, V. V.; Ovsyannikov, S. V. *J. Phys.: Condens. Matter* **2009**, *21*, 271001.

(82) Pinto, H. P.; Elliott, S. D. *J. Phys.: Condens. Matter* **2006**, *18*, 10427–10436.

(83) Mantovan, R.; Lamperti, A.; Georgieva, M.; Tallarida, G.; Fanciulli, M. *J. Phys. D* **2010**, *43*, 065002.

(84) Zhang, M.; Yan, H.; Yan, H. *J. Magn. Magn. Mater.* **2009**, *321*, 2340–2344.

(85) Zhang, D. H.; Liu, Z. Q.; Han, S.; Li, C.; Lei, B.; Stewart, M. P.; Tour, J. M.; Zhou, C. W. *Nano Lett.* **2004**, *4*, 2151–2155.

(86) Yoon, K. S.; Koo, J. H.; Do, Y. H.; Kim, K. W.; Kim, C. O.; Hong, J. P. *J. Magn. Magn. Mater.* **2005**, *285*, 125–129.

(87) Parkinson, G. S.; Mulakaluri, N.; Losovyj, Y.; Jacobson, P.; Pentcheva, R.; Diebold, U. *Phys. Rev. B* **2010**, *82*, 125413.

(88) Kurahashi, M.; Sun, X.; Yamauchi, Y. *Phys. Rev. B* **2010**, *81*, 193402.

(89) Lodziana, Z. *Phys. Rev. Lett.* **2007**, *99*, 206402.

(90) Pentcheva, R.; Wendler, F.; Meyerheim, H. L.; Moritz, W.; Jedrecy, N.; Scheffler, M. *Phys. Rev. Lett.* **2005**, *94*, 126101.

(91) Dudarev, S. L.; Botton, G. A.; Savrasov, S. Y.; Humphreys, C. J.; Sutton, A. P. *Phys. Rev. B* **1998**, *57*, 1505–1509.

(92) Rakhecha, V. C.; Murthy, N. S. S. *J. Phys. C* **1978**, *11*, 4389–4404.

(93) Goering, E.; Gold, S.; Lafkioti, M.; Schutz, G. *Europhys. Lett.* **2006**, *73*, 97–103.

(94) Heaton-Burgess, T.; Yang, W. T. *J. Chem. Phys.* **2010**, *132*, 234113.

(95) Mori-Sanchez, P.; Cohen, A. J.; Yang, W. T. *J. Chem. Phys.* **2006**, *125*, 201102.

(96) Perdew, J. P.; Parr, R. G.; Levy, M.; Balduz, J. L. *Phys. Rev. Lett.* **1982**, *49*, 1691–1694.

(97) Mori-Sanchez, P.; Cohen, A. J.; Yang, W. T. *Phys. Rev. Lett.* **2008**, *100*, 146401.

(98) Chevrier, V. L.; Ong, S. P.; Armiento, R.; Chan, M. K. Y.; Ceder, G. *Phys. Rev. B* **2010**, *82*, 075122.

(99) van der Marel, D.; Sawatzky, G. A. *Phys. Rev. B* **1988**, *37*, 10674–10684.

(100) Cohen, A. J.; Mori-Sanchez, P.; Yang, W. T. *J. Chem. Phys.* **2007**, *126*, 191109.

(101) Krukau, A. V.; Vydrov, O. A.; Izmaylov, A. F.; Scuseria, G. E. *J. Chem. Phys.* **2006**, *125*, 224106.

(102) Paier, J.; Marsman, M.; Hummer, K.; Kresse, G.; Gerber, I. C.; Angyan, J. G. *J. Chem. Phys.* **2006**, *125*, 249901.

(103) Paier, J.; Marsman, M.; Hummer, K.; Kresse, G.; Gerber, I. C.; Angyan, J. G. *J. Chem. Phys.* **2006**, *124*, 154709.

(104) Oshio, H.; Hoshino, N.; Ito, T.; Nakano, M. *J. Am. Chem. Soc.* **2004**, *126*, 8805–8812.

(105) Oshio, H.; Hoshino, N.; Ito, T. *J. Am. Chem. Soc.* **2000**, *122*, 12602–12603.

(106) Vosko, S. H.; Wilk, L.; Nusair, M. *Can. J. Phys.* **1980**, *58*, 1200–1211.

(107) Perdew, J. P.; Chevary, J. A.; Vosko, S. H.; Jackson, K. A.; Pederson, M. R.; Singh, D. J.; Fiolhais, C. *Phys. Rev. B* **1992**, *46*, 6671–6687.

(108) Bogani, L.; Wernsdorfer, W. *Nat. Mater.* **2008**, *7*, 179–186.

(109) Oshio, H.; Nakano, M. *Chem.—Eur. J.* **2005**, *11*, 5178–5185.

(110) Ribas-Arino, J.; Baruah, T.; Pederson, M. R. *J. Am. Chem. Soc.* **2006**, *128*, 9497–9505.

(111) De Vos, D. E.; Alaerts, L.; Seguin, E.; Poelman, H.; Thibault-Starzyk, F.; Jacobs, P. A. *Chem.—Eur. J.* **2006**, *12*, 7353–7363.

(112) Walton, K. S.; Karra, J. R. *Langmuir* **2008**, *24*, 8620–8626.

(113) Prestipino, C.; Regli, L.; Vitillo, J. G.; Bonino, F.; Damin, A.; Lamberti, C.; Zecchina, A.; Solari, P. L.; Kongshaug, K. O.; Bordiga, S. *Chem. Mater.* **2006**, *18*, 1337–1346.

(114) Schlichte, K.; Kratzke, T.; Kaskel, S. *Microporous Mesoporous Mater.* **2004**, *73*, 81–88.

(115) Thomas, K. M.; Xiao, B.; Wheatley, P. S.; Zhao, X. B.; Fletcher, A. J.; Fox, S.; Rossi, A. G.; Megson, I. L.; Bordiga, S.; Regli, L.; Morris, R. E. *J. Am. Chem. Soc.* **2007**, *129*, 1203–1209.

(116) Liu, Y.; Xiang, S. C.; Zhou, W.; Gallegos, J. M.; Chen, B. L. *J. Am. Chem. Soc.* **2009**, *131*, 12415–12419.

(117) Poppl, A.; Kunz, S.; Himsl, D.; Hartmann, M. *J. Phys. Chem. C* **2008**, *112*, 2678–2684.

(118) Zhang, X. X.; Chui, S. S. Y.; Williams, I. D. *J. Appl. Phys.* **2000**, *87*, 6007–6009.

(119) Bohlmann, W.; Poppl, A.; Sabo, M.; Kaskel, S. *J. Phys. Chem. B* **2006**, *110*, 20177–20181.

(120) Nakatsuji, H.; Hada, M.; Ehara, M.; Toyota, K.; Fukuda, R.; Hasegawa, J.; Ishida, M.; Nakajima, T.; Honda, Y.; Kitao, O.; Nakai, H. *SAC/SAC-CI Program Combined with Gaussian for Calculating Ground, Excited, Ionized, and Electron-Attached States and Singlet, Doublet, Triplet, Quartet, Quintet, Sextet, and Septet Spin States and Their Analytic Energy Gradients*; Kyoto University: Kyoto, Japan, 2005; pp 1−450.

(121) Tyuterev, V. G.; Tashkun, S.; Jensen, P.; Barbe, A.; Cours, T. *J. Mol. Spectrosc.* **1999**, *198*, 57–76.

(122) Bacis, R.; Bouvier, A. J.; Flaud, J. M. *Spectrochim. Acta, Part A* **1998**, *54*, 17–34.

(123) Bouvier, A. J.; Inard, D.; Veyret, V.; Bussery, B.; Bacis, R.; Churassy, S.; Brion, J.; Malicet, J.; Judge, R. H. *J. Mol. Spectrosc.* **1998**, *190*, 189–197.

(124) Willitsch, S.; Innocenti, F.; Dyke, J. M.; Merkt, F. *J. Chem. Phys.* **2005**, *122*, 024311.

(125) Bultinck, P.; Cooper, D. L.; Van Neck, D. *Phys. Chem. Chem. Phys.* **2009**, *11*, 3424–3429.